

# First evaluation of the GEMS glyoxal products against TROPOMI and ground-based measurements

Eunjo S. Ha<sup>1</sup>, Rokjin J. Park<sup>1</sup>, Hyeong-Ahn Kwon<sup>2</sup>, Gitaek T. Lee<sup>1</sup>, Sieun D. Lee<sup>1</sup>, Seunga Shin<sup>1</sup>, Dong-Won Lee<sup>3</sup>, Hyunkee Hong<sup>3</sup>, Christophe Lerot<sup>4\*</sup>, Isabelle De Smedt<sup>4</sup>, [Thomas Danckaert<sup>4</sup>](#),  
5 Francois Hendrick<sup>4</sup>, and Hitoshi Irie<sup>5</sup>

<sup>1</sup>School of Earth and Environmental Science, Seoul National University, Seoul, Republic of Korea

<sup>2</sup>Department of Environmental & Energy Engineering, The University of Suwon, Suwon, Republic of Korea

<sup>3</sup>National Institute of Environmental Research, Incheon, Republic of Korea

<sup>4</sup>Royal Belgian Institute for Space Aeronomy (BIRA-IASB), Brussels, Belgium

10 <sup>5</sup>Department of Earth Sciences, Chiba University, Chiba, Japan

\*Now at Constellr, Brussels, Belgium

*Correspondence to:* Rokjin J. Park ([rjpark@snu.ac.kr](mailto:rjpark@snu.ac.kr)) and Hyeong-Ahn Kwon ([hakwon@suwon.ac.kr](mailto:hakwon@suwon.ac.kr))

**Abstract.** The Geostationary Environment Monitoring Spectrometer (GEMS) aboard the GEO-KOMPSAT-2B satellite is the first geostationary satellite launched to monitor the environment. GEMS conducts hourly measurements during the day  
15 over East and Southeast Asia. This work presents glyoxal (CHOCHO) vertical column densities (VCDs) retrieved from GEMS, with optimal settings for glyoxal retrieval based on sensitivity tests involving reference spectrum sampling and fitting window selection. We evaluated GEMS glyoxal VCDs by comparing them to TROPOMI and MAX-DOAS ground-based observations. On average, GEMS and TROPOMI VCDs show a spatial correlation coefficient of 0.63, increasing to  
20 0.87 for Northeast Asia. While GEMS and TROPOMI demonstrate similar monthly variations in the Indochinese peninsula regions ( $R > 0.67$ ), variations differ in other areas. Specifically, GEMS VCDs are ~~lower in the summer and~~ higher in the winter ~~than~~  
~~and either lower or comparable to~~ TROPOMI ~~and MAX-DOAS~~ VCDs in ~~the summer across~~ Northeast Asia, ~~potentially due~~. We attributed the discrepancies in the monthly variation to a polluted reference spectrum and high NO<sub>2</sub> concentrations. ~~This trend also occurs in comparing monthly variations between~~ When we correct GEMS ~~and MAX-DOAS~~  
~~VCDs~~ glyoxal VCDs as a function of NO<sub>2</sub> SCDs, the monthly correlation coefficients substantially increase from 0.16–0.40  
25 to 0.45–0.72 in high NO<sub>2</sub> regions. When averaged hourly, GEMS and MAX-DOAS VCDs exhibit similar diurnal variations, especially at stations in Japan (Chiba, Kasuga, and Fukue).

## 1 Introduction

Glyoxal (CHOCHO) is the smallest di-carbonyl compound with a short atmospheric lifetime of fewer than 3 hours during daylight hours (Volkamer et al., 2006). Some glyoxal is directly emitted through biomass burning and biofuel  
30 utilization; however, the majority is produced via the oxidation of non-methane volatile organic compounds (NMVOCs) (Fu

et al., 2008). Glyoxal is predominantly removed from the atmosphere by photolysis and reaction with OH radicals (Volkamer et al., 2005). When glyoxal oxidizes in the presence of nitrogen oxides, it contributes to the secondary formation of ozone. Furthermore, the high solubility of glyoxal facilitates its absorption by aqueous aerosols and cloud droplets, forming secondary organic aerosols (SOAs) (Fu et al., 2008; Lerot et al., 2021). Given that ozone and SOAs are harmful air pollutants and agents of climate change, comprehending their VOC precursors is critical for managing air quality and climate.

The number of VOCs detectable from space is limited compared to the numerous VOCs existing in the atmosphere. Glyoxal and formaldehyde (HCHO) are examples of non-methane volatile organic compounds (NMVOCs) that are retrieved using ultraviolet (UV) to visible ~~wavelength~~wavelengths. These compounds, predominantly produced by the oxidation of other VOCs and characterized by short atmospheric lifetimes, provide valuable insights into local VOC emissions when measured. Satellite observations offer a comprehensive overview for estimating top-down emissions due to their extensive spatial coverage compared to ground-based, in situ measurements (Choi et al., 2022). The different yields of formaldehyde and glyoxal from NMVOCs add additional information to constrain individual NMVOC emissions. For example, formaldehyde is typically produced in large amounts from alkenes, while glyoxal is a high-yield product of aromatic compounds (~~(Dufour et al., 2009;~~ Cao et al., 2018; Chan Miller et al., 2016); Dufour et al., 2009). Chan Miller et al. (2017) noted that while formaldehyde and glyoxal data are closely linked, the precise measurements of glyoxal could provide additional information, especially in environments with low nitrogen oxides (NO<sub>x</sub>). Furthermore, due to the shorter atmospheric lifetime of glyoxal compared to formaldehyde, elevated concentrations of glyoxal are indicative of the immediate vicinity of wildfires and areas with intense photochemical reactions (Alvarado et al., 2020; ~~(Vrekoussis et al., 2010;~~ Alvarado et al., 2020). The ratio of glyoxal to formaldehyde ( $RGF = [CHOCHO]/[HCHO]$ ) has been used in several studies to differentiate the origins of VOC emissions, distinguishing between anthropogenic or biogenic sources (Digangi et al., 2012; ~~(Vrekoussis et al., 2010;~~ Digangi et al., 2012).

The observation of glyoxal from a sun-synchronous satellite was conducted by the SCanning Imaging Absorption spectroMeter for Atmospheric CHartographY (SCIAMACHY) instrument, which was launched in 2002 (Wittrock et al., 2006). This instrument has a pixel size of 60 km along the track and 120 km across the track, enabling global coverage in six days. Building upon SCIAMACHY's achievements, glyoxal columns with improved spatial and temporal resolutions have been retrieved from the Global Ozone Monitoring Experiment-2 (GOME-2) (Lerot et al., 2010; Vrekoussis et al., 2009) and Ozone Monitoring Instrument (OMI) (~~Alvarado(Chan Miller~~ et al., 2014; AlvaradoChan Miller et al., 2014). The spatial resolutions for GOME-2 and OMI glyoxal data are  $80 \times 40 \text{ km}^2$  and  $13 \times 24 \text{ km}^2$ , respectively, offering global coverage in 1.5 days and one day. Glyoxal columns retrieved from the TROPOspheric Monitoring Instrument (TROPOMI) exhibit the highest spatial resolution, at  $3.5 \times 5.5 \text{ km}^2$ , with an overpass of 13:30 local time (Lerot et al., 2021). These Low Earth Orbit (LEO) satellite instruments have significantly contributed to mapping the spatial distribution of glyoxal globally. However,

they are limited in their ability to capture the diurnal variations of glyoxal, which are crucial for understanding its emissions, transport, and chemical reactions.

65 To address the limitations of sun-synchronous satellites, the Geostationary Environment Monitoring Spectrometer (GEMS) was launched aboard the GEO-KOMPSAT-2B satellite in February 2020 (Kim et al., 2020), providing trace gas and aerosol measurements as the first geostationary satellite. GEMS performs hourly measurements across East and Southeast Asia, including parts of India, ranging from 6–10 times a day depending on the season. This study presents the retrieval of glyoxal data from GEMS using an algorithm that Kwon et al. (2019) developed for formaldehyde retrieval. The  
70 adaptation of this algorithm for glyoxal retrieval is detailed in Sect. 2. We examine the retrieval uncertainty in Sect. 3. We evaluate the GEMS glyoxal product by comparing it with TROPOMI data in Sect. 34, and GEMS glyoxal products are validated against ground-based observations in Sect. 45.

## 2 Description of the GEMS glyoxal algorithm

For glyoxal retrievals, we use the same retrieval algorithm for formaldehyde for GEMS, and detailed descriptions of  
75 the algorithm are explained in Kwon et al. (2019) and Lee et al. (2023-Preprint2024). Here, we only focus on the distinctive features of glyoxal retrievals. The algorithm descriptions and the evaluation results in this paper are based on GEMS glyoxal V2.0, which has been the operational product since 2023. The GEMS system attributes and parameters for radiance fitting are summarized in Table 1. Retrieving GEMS glyoxal vertical column densities (VCDs) involves three steps. First, a radiative transfer equation is fitted to back-scattered radiances within a glyoxal's spectral absorption range. This spectral  
80 fitting process yields a glyoxal slant column density (SCD), representing the integrated concentration along the mean photon path. Subsequently, the SCD is converted to the VCD by dividing by the air mass factor (AMF). AMF converts SCD to VCD by accounting for the light path varying with viewing geometry, the atmospheric scattering from clouds, and the vertical profile of glyoxal. Lastly, background correction is performed by adding simulated concentration over the reference sector.

Glyoxal is a weak absorber within ~~theits~~ absorption range ~~of glyoxal~~ compared to ozone and nitrogen dioxide, and  
85 the amount of glyoxal in the atmosphere is relatively ~~small~~low. Therefore, strong absorbers and instrument noise can significantly constrain glyoxal retrievals. ~~We~~The native spatial resolution of GEMS is  $3.5 \times 8 \text{ km}^2$ , with nitrogen dioxide, ozone, formaldehyde, and aerosol products retrieved at this resolution. For the weaker absorbers, we use co-added products ~~with 16 (4×4) GEMS pixels to enhance the signal to noise ratio for GEMS glyoxal retrievals~~, including radiance, irradiance, surface reflectance, and cloud products. Specifically, we co-add products with 4 (2×2) and 16 (4×4) GEMS pixels to retrieve  
90 sulfur dioxide and glyoxal, respectively, to enhance the signal-to-noise ratio. This approach reduces ~~at~~ the spatial resolution ~~of~~ to about  $14 \times 32 \text{ km}^2$  for glyoxal over Seoul, South Korea, but results in the stable spectral fitting to obtain glyoxal SCDs.

## 2.1 Spectral fitting

The spectral fitting yields glyoxal SCDs by fitting the modeled radiative transfer equation to measured radiances, ~~as described in Eq. (6) by Kwon et al. (2019).~~ The modeled radiative transfer equation demonstrates the attenuation of the reference spectrum by gas absorptions based on the Lambert-Beer law (Kwon et al., 2019) and can be expressed as follows:

$$I(\lambda) = [(aI_0(\lambda) + c_r\sigma_r(\lambda)) e^{-\sum_i SCD_i\sigma_i(\lambda)} + c_{cm}\sigma_{cm}(\lambda)]P_{sc}(\lambda) + P_{bl}(\lambda). \quad (1)$$

In Eq. (1),  $a$  represents an amplification factor applied to the reference spectrum  $I_0(\lambda)$ ;  $c_r\sigma_r(\lambda)$  accounts for the contribution of the Ring effect; the term  $e^{-\sum_i SCD_i\sigma_i(\lambda)}$  characterizes the attenuation of light by absorbing species  $i$ ;  $c_{cm}\sigma_{cm}(\lambda)$  reflects the influence of the common mode; and  $P_{sc}(\lambda)$  and  $P_{bl}(\lambda)$  stand for scaling and baseline polynomials, respectively. Solar irradiance is commonly used as the reference spectrum in the UV to visible wavelengths. However, using solar irradiance to retrieve weak absorbers could result in systematic biases caused by spectral interference or instrumental limitations (Lerot et al., 2021). Therefore, we use measured radiances as the reference spectrum in the spectral fitting. We obtain the reference spectrum by averaging radiances from clean pixels for the past three days for each track and scene in the reference sector (120–150° E). This reference sector contains open oceans where interference of liquid water absorption occurs, which could lead to a high bias of glyoxal VCDs on land. However, we inevitably selected this region as a reference sector since it generally shows low concentrations of glyoxal and other pollutants.

The spectral fitting accounts for absorption by chemical species, including CHOCHO, NO<sub>2</sub>, O<sub>3</sub>, O<sub>4</sub>, H<sub>2</sub>O (liquid), and H<sub>2</sub>O (vapor). In addition, the GEMS instrument's polarization sensitivity is included as a pseudo-absorber since GEMS is not equipped with a polarization scrambler. The polarization sensitivity values measured before the launch of the GEMS are depicted in Figure 5 of Lee et al. (2023 Preprint2024). The polarization sensitivity values at the fitting window of glyoxal are incorporated for the spectral fitting. We use the most updated absorption cross-sections available as of now. NO<sub>2</sub> absorption cross-sections at two temperatures (220, 294 K) are used, considering the strong influence of NO<sub>2</sub> at the glyoxal absorption range (Table 1).

Glyoxal retrieval is highly sensitive to the selection of the fitting window due to its low optical depth in the atmosphere (Alvarado et al., 2014). ~~We tested fitting windows that included glyoxal's absorption wavelength and selected an optimal fitting window of 433.0–461.5 nm. This fitting window generally showed low fitting RMS and column uncertainty over the domain, low column amounts in oceans and deserts, and higher column amounts where glyoxal sources exist.~~ We conduct sensitivity tests of fitting window selection to minimize fitting RMS and column uncertainty of the retrieved glyoxal averaged over the entire domain by varying lower and upper wavelengths with 0.5 nm increments. Figure 1 shows the results of our sensitivity tests and our optimal fitting window of 433.0–461.5 nm for glyoxal retrieval. The fitting window of 433.0–461.5 nm was selected considering its low fitting RMS and column uncertainty. However, we find that the differential slant column densities (dSCDs) over the reference sector (120–150° E) retrieved with this fitting window have a positive value, which could result in a high systematic bias, which we discuss below.

125 Figures [1a2a](#) and [1b2b](#) show glyoxal SCDs and root-mean-square values of spectral fitting residuals (fitting RMS) retrieved using radiance references. The 1<sup>st</sup> and 99<sup>th</sup> percentiles and ~~an~~<sup>the</sup> average of fitting RMS in August 2020 are  $3.6 \times 10^{-4}$ ,  $8.0 \times 10^{-4}$ , and  $5.6 \times 10^{-4}$ , respectively. The fitting RMS are large over the Tibetan plateau and the southwestern part of the domain despite low VCDs, indicating the low credibility of the retrieval. Figure [1e2c](#) shows one case of fitted optical depth and fitting residuals in Indonesia (15 August 2020; 0.6° N, 123.9° E). The fitting residuals oscillate centered along the optical depth, indicating that fitting residuals have no specific features.

130

**Table 1. Summary of operational GEMS system attributes and parameters for radiance fitting.**

GEMS system attributes	Spectral range	300 – 500 nm
	Spectral resolution	< 0.6 nm
	Wavelength sampling	< 0.2 nm
	Field of regard (FOR)	≥ 5000 (N/S) km × 5000 (E/W) km (5° S–45° N, 75–145° E)
	Spatial resolution (at Seoul)	< <del>-14 km</del> × <del>32 km</del> for glyoxal (4 × 4 co-added pixels)
	Duty cycle	6 ~ 10 times per day (six times in winter, ten times in summer)
	Imaging time	≤ 30 min
Radiance fitting parameters	Fitting window (calibration window) <sup>1</sup>	433.0–461.5 nm (431. <del>03</del> –463.5 nm)
	Reference	Three days average of measured radiances from easternmost swaths (120–150° E) under clear-sky <del>condition</del> <sup>conditions</sup> (cloud fraction < 0.4)
	Solar reference spectrum	Chance and Kurucz (2010)
	Absorption cross-sections	CHOCHO at 296 K (Volkamer et al., 2005) O <sub>3</sub> at 223 K (Serdyuchenko et al., 2014) NO <sub>2</sub> at 220 K and 294 K (Vandaele et al., 1998)

<sup>1</sup>. The calibration window refers to the wavelength range used for the calibration. During calibration, a convolved solar reference spectrum is fitted to the measured irradiances and radiances to obtain wavelength shift parameters and polynomial parameters (Kwon et al., 2019).

		O <sub>4</sub> at 293 K (Finkenzeller and Volkamer, 2022) H <sub>2</sub> O (vapor) at 283 K (Gordon et al., 2022) H <sub>2</sub> O (liquid) at 296 K (Mason et al., 2016)
	Ring effect	Chance and Kurucz (2010)
	Common mode	Online common mode from easternmost swaths (120–150° E) for a day
	Polarization correction	Polarization sensitivity vector at the central pixel of charge-coupled-device (CCD)
	Scaling and baseline polynomials	Third order

## 2.2 Air mass factor

In the presence of atmospheric scattering, AMF can be formulated in terms of scattering weight ( $w_z$ ) and vertical shape factor ( $S_z$ ) (Palmer et al., 2001):

$$AMF = \int_0^{\infty} w_z S_z dz \quad (2)$$

Scattering weight is a function of the solar zenith angle, viewing zenith angle, relative azimuth angle, surface reflectance, cloud pressure, and cloud fraction. We use different values of these parameters for each latitude, longitude, and month. A look-up table of the scattering weight at 448 nm is constructed using VLIDORT v2.6 (Spurr, 2006). Surface reflectance is obtained from OMI Lambertian Equivalent Reflectance (LER) Climatology products (Kleipool, 2010), and cloud pressure and fraction are obtained from GEMS L2 cloud products.

The vertical shape factor is calculated using a global 3-D chemical transport model (GEOS-Chem v13.0.0) with 47 vertical layers and 0.25°×0.3125° horizontal resolutions in Asia (Bey et al., 2001; Wang et al., 2004). The KORUS v5 inventory was used for anthropogenic emissions (Woo et al., 2020). Biogenic emissions are taken from MEGANv2.1 (Guenther et al., 2012), and biomass burning emissions are taken from the monthly GFED4 inventory (van der Werf et al., 2010). We use monthly mean hourly vertical profiles from August 2020 to July 2021 to better represent diurnal variations.

## 2.3 Background correction

Glyoxal SCDs retrieved from the spectral fitting using the radiance reference are differential slant column densities (dSCDs) that do not include background columns over the clean reference sector (120–150° E). Therefore, we use simulated vertical columns in the reference sector for background correction, as shown in Eq. (2):

$$VCD(i, j) = \frac{SCD(i, j)}{AMF(i, j)} = \frac{dSCD(i, j) + AMF_0(lat) VCD_m(lat)}{AMF(i, j)} \quad (3)$$

155 AMF(*i,j*) indicates the AMF at the *i*th cross-track (north-south direction) and *j*th along-track (east-west direction) positions, and AMF<sub>0</sub>(lat) denotes the AMF over the reference sector. VCD<sub>m</sub> is simulated monthly mean hourly VCD zonally averaged in the reference sector (120–150° E) from the model used to construct AMF. Figure 23 shows glyoxal VCDs with and without background correction. The difference is large in the high latitudes where the reference sector is close to polluted sources. However, the background contribution shown in Figure 2e3c is lower than the offset value (10<sup>14</sup> molecules cm<sup>-2</sup>) used for the background correction of the TROPOMI (Lerot et al., 2021) and SCIAMACHY (Wittrock, 2006) glyoxal column. The offset value of 10<sup>14</sup> molecules cm<sup>-2</sup> is selected from the ship-based measurement over the Pacific Ocean (Sinreich et al., 2010). As the background contribution for GEMS glyoxal VCD is low, the VCDs with (Figure 2a3a) and without background correction (Figure 2b3b) do not represent significant differences. The low value of VCD<sub>m</sub> is due to the underestimation of glyoxal columns from the current chemical transport models (CTM) (Li et al., 2018; Silva et al., 2018). Simulated glyoxal VCDs from the ECHAM/MESSy Atmospheric Chemistry (EMAC) model also showed lower values than airborne measurements from the EMerGe-Asia campaign observing the East China Sea in early spring 2018 (Kluge et al., 2023). Previous studies suggested that the emissions of precursor VOCs are underestimated (Choi et al., 2022; Kwon et al., 2021; Choi et al., 2022) and that the oxidative chemistry producing glyoxal is not well represented (Silva et al., 2018).

### 2.3 Uncertainty analysis

170 In this section, we examine the uncertainty of each retrieval step. Assuming that each retrieval step is uncorrelated, the total uncertainty in the retrieval can be expressed as the sum of the uncertainties of each retrieval step (Boersma et al., 2004; Kwon et al., 2019; De Smedt et al., 2018):

$$\sigma_{VCD}^2 = \left( \frac{\partial VCD}{\partial SCD} \sigma_{SCD} \right)^2 + \left( \frac{\partial VCD}{\partial AMF} \sigma_{AMF} \right)^2 + \left( \frac{\partial VCD}{\partial VCD_m} \sigma_{VCD_m} \right)^2 + \left( \frac{\partial VCD}{\partial AMF_0} \sigma_{AMF_0} \right)^2 \quad (4)$$

where  $\sigma$  denotes uncertainty in each parameter. Using the relationship shown in Eq. (3), we can derive the sensitivity of VCDs to each parameter, resulting in the conversion of Eq. (4) as follows:

175 
$$\sigma_{VCD}^2 = \frac{1}{AMF^2} \sigma_{SCD}^2 + \frac{SCD^2}{AMF^4} \sigma_{AMF}^2 + \frac{AMF_0^2}{AMF^2} \sigma_{VCD_m}^2 + \frac{VCD_m^2}{AMF^2} \sigma_{AMF_0}^2 \quad (5)$$

Uncertainty in each parameter includes both random and systematic components. Unlike systematic uncertainty, random uncertainty decreases for a spatial or temporal averaging in the ratio of  $\frac{1}{\sqrt{N}}$ , where N is the number of pixels averaged. In this study, we only consider random uncertainty in slant columns as random uncertainty in AMF and VCD<sub>m</sub> are difficult to separate from the systematic uncertainty in practice.

## 180 3.1 Uncertainties in slant columns

### 3.1.1 Random uncertainties and observation noise in slant columns

Random uncertainties in slant columns ( $\sigma_{\bar{s}}\sigma_{SCD,rand}$ ) are fitting uncertainties mainly resulting from instrument noise and can be calculated using Eq. (15) of (Kwon et al., 2019):

$$\sigma_{\bar{s}}^2\sigma_{SCD,rand,j}^2 = RMS^2 \frac{m}{m-n} C_{j,j} C_{j,j} \quad (6)$$

185 RMS is the root-mean-square value of fitting residuals,  $m$  and  $n$  are the number of spectral grids and fitting parameters,  $C_{j,j}$  are diagonal components of a covariance matrix, and  $j$  is the subscript for fitting parameters. The 1<sup>st</sup> to the 99<sup>th</sup> percentiles of random uncertainties are  $3.6 \times 10^{14}$  and  $1.6 \times 10^{15}$  molecules  $\text{cm}^{-2}$  in August 2020, with a mean of  $8.6 \times 10^{14}$  molecules  $\text{cm}^{-2}$ . The random uncertainties of GEMS are higher than TROPOMI, as the 1<sup>st</sup> to the 99<sup>th</sup> percentiles of TROPOMI random uncertainties are  $4.4 \times 10^{14}$  and  $1.0 \times 10^{15}$  molecules  $\text{cm}^{-2}$  in August 2020 with a mean of  $6.5 \times 10^{14}$  molecules  $\text{cm}^{-2}$  in the GEMS field of regards (FOR).

The observation noise is large compared to the actual signal for glyoxal retrieval, and the credibility of glyoxal retrieval is known to be low in oceans due to low concentration and interference with liquid water absorption (Alvarado et al., 2014). Figure 34 illustrates VCDs over the Pacific Ocean and the observation noise estimated from its standard deviation. We followed the analysis from Lerot et al. (2021) to estimate the noise level of GEMS VCDs and compared them with TROPOMI VCDs. While Lerot et al. (2021) analyzed VCDs over 180–120° W, we analyzed GEMS VCDs over 130–146° E due to the limited coverage of the geostationary satellite. We filter out pixels over land with cloud cover (cloud fraction > 0.4) for the analysis. VCDs binned in 5° latitude bands range from  $0.9 \times 10^{14}$  to  $2.1 \times 10^{14}$  molecules  $\text{cm}^{-2}$ , which is notably lower than the scatter for all data. GEMS glyoxal observation noise ranges from  $3.7 \times 10^{14}$  to  $7.0 \times 10^{14}$  molecules  $\text{cm}^{-2}$ , comparable to the noise of TROPOMI VCDs.

200 3

### 3.1.2 Systematic uncertainties in slant columns

Systematic uncertainties in slant columns are associated with various factors such as wavelength calibration, bandpass function, residual stray light, and absorption cross-sections. We assessed the uncertainty resulting from absorption cross-section, as it is a preeminent factor contributing to the uncertainty in slant columns (Lerot et al., 2021; De Smedt et al., 2018). The uncertainty related to absorption cross-section ( $\sigma_{SCD,abs}^2$ ) is estimated by matrix analysis, following Rodgers formalism (Rodgers, 2000):

$$\sigma_{SCD,abs}^2 = \sum_{j=1}^n dSCD_j^2 [GS_{bj}G] \quad (7)$$

where  $j (=1, \dots, n)$  is the subscript for absorbing species;  $G$  is the matrix formed by  $G = [K^T K]^{-1} K^T$ , where  $K$  is the matrix constructed from the absorption cross-sections with the dimension of  $m \times n$  ( $m$  is the number of spectral grids);  $S_{bj}$  ( $n \times n$ ) is



210 the cross-section error covariance matrix. The diagonal components of  $S_{bj}$  are assigned based on the uncertainties for the  
absorption cross-sections of each species: glyoxal (3%) (Volkamer et al., 2005),  $\text{NO}_2$  (3%) (Vandaele et al., 1998),  $\text{O}_3$   
(2.6%) (Serdyuchenko et al., 2014), gas phase  $\text{H}_2\text{O}$  (4%) (Gordon et al., 2022), and  $\text{O}_4$  (3%) (Finkenzeller and Volkamer,  
2022). The contribution of liquid water absorption is excluded in the calculation, as it had higher contributions than  $2 \times 10^{15}$   
215 liquid water. Using this reference sector for liquid water retrieval results in negative dSCDs with large absolute values over  
land, which could lead to a large contribution from the liquid water absorption cross-section. The dSCDs for each species are  
retrieved for March 2021.

For geostationary satellites, a radiance reference is required for every along-track, but the observation area is  
limited to certain regions such as Asia, North America, and Europe. As a result, the reference sector inevitably includes  
220 polluted regions, and the selection of the reference sector significantly influences retrieval results. Therefore, we examine the  
systematic uncertainty arising from the current reference sector. Since October 2020, scan areas have been fixed to Half East  
(HE), Half Korea (HK), Full Central (FC), and Full West (FW). The easternmost longitude of HE, HK, FC, and FW scan  
areas are  $152^\circ$  E,  $142^\circ$  E,  $142^\circ$  E, and  $133^\circ$  E, respectively. Therefore, relatively more clean areas in the Pacific Ocean are  
not observed in the HK, FC, and FW scan areas. However, during the in-orbit test period (IOT) from August to September  
225 2020, observations were frequently taken as Nominal daily scan, which covers  $90\text{--}150^\circ$  E (Figure 1 of Kwon et al., 2019).  
This enables us to obtain the reference spectrum over  $120\text{--}150^\circ$  E during the IOT. Figure 5 demonstrates the sensitivity of  
retrieved glyoxal VCDs to the selection of reference spectrum depending on the scan areas in August 2020. Figure 5a  
illustrates glyoxal VCDs retrieved with the reference spectrum taken from the reference sector of  $120\text{--}150^\circ$  E in August  
2020. Figure 5b shows the same retrieved glyoxal VCDs but with the reference spectrum averaged over  $120\text{--}133^\circ$  E, which  
230 is the narrow reference sector limited by the FW scan, frequently conducted after the IOT. VCDs in Figure 5b are about 22%  
lower on average than those in Figure 5a, possibly due to the effect of local pollution on the reference spectrum. We  
assumed the systematic uncertainty associated with the reference spectrum as the standard deviation of the difference in SCD  
retrieved from the reference sector of  $120\text{--}133^\circ$  E and  $120\text{--}150^\circ$  E averaged for the observations in August 2020.

Figure 6a shows the total systematic uncertainty in SCD and the contribution from each uncertainty source relative  
235 to glyoxal SCD. The contribution from the absorption cross-section of species  $j$  is calculated as  $\sqrt{d\text{SCD}_j^2 [GS_{bj}G]}$ . For most  
latitudes, uncertainty associated with the reference sector represented the largest ratio, followed by the uncertainties  
associated with  $\text{NO}_2$  and  $\text{O}_3$  absorption cross-sections. Figure 6b illustrates the contribution of SCD, AMF, and background  
correction to the uncertainty in VCD. The uncertainty in VCD is dominated by the uncertainty in SCD.

### 240 **3.2 Uncertainty in AMF**

We estimate the uncertainty in AMF by the composite of uncertainties in surface albedo ( $\alpha_s$ ), cloud top pressure ( $p_c$ ), effective cloud fraction ( $f_c$ ), and profile height parameter ( $p_h$ ) (Kwon et al., 2019):

$$\sigma_{AMF}^2 = \left(\frac{\partial AMF}{\partial \alpha_s} \sigma_{\alpha_s}\right)^2 + \left(\frac{\partial AMF}{\partial p_c} \sigma_{p_c}\right)^2 + \left(\frac{\partial AMF}{\partial f_c} \sigma_{f_c}\right)^2 + \left(\frac{\partial AMF}{\partial p_h} \sigma_{p_h}\right)^2, \quad (8)$$

245 where  $p_h$  is defined as the height below which 75% of glyoxal VCDs exist from the surface. The uncertainties  $\sigma_{\alpha_s}$ ,  $\sigma_{p_c}$ , and  $\sigma_{f_c}$  are assigned as 0.02, 50hPa, and 0.05, respectively (De Smedt et al., 2018; Kwon et al., 2019). The uncertainty  $\sigma_{p_h}$  is calculated as a standard deviation of  $p_h$  of a priori profile, ranging from 68hPa to 293hPa for different latitudes. The sensitivities of each parameter to AMF are obtained from the look-up table of the scattering weight at 448 nm. Uncertainties in AMF contribute 7–14% to the uncertainties in VCD across the latitudes.

### 250 **3.3 Uncertainty in background correction**

The contribution of background correction to the total uncertainty in VCD can be expressed as the sum of the third and fourth terms on the right-hand side of Eq. (5). We assign the uncertainty in simulated background concentration ( $\sigma_{VCD_m}$ ) as the standard deviation of simulated concentration for each latitude.  $\sigma_{VCD_m}$  ranges from  $2.5 \times 10^{12}$  to  $1.9 \times 10^{13}$  molecules  $\text{cm}^{-2}$ , and  $VCD_m$  ranges from  $2.5 \times 10^{12}$  to  $2.6 \times 10^{13}$  molecules  $\text{cm}^{-2}$ . The uncertainties in background  
255 correction represent lower values than those in SCD and AMF for most latitudes. The uncertainties in background correction represent relatively high values in the latitudes lower than  $0^\circ$  N and higher than  $28^\circ$  N, where the terrestrial sources influence the reference sector. The total systematic uncertainties in VCD range from 33% to 61%, which is comparable to the 30% to 70% uncertainty range in TROPOMI glyoxal VCDs (Lerot et al., 2021).

### 260 **4 Comparison with TROPOMI data**

We evaluate GEMS glyoxal retrieval by comparing GEMS glyoxal VCDs with TROPOMI from August 2020 to July 2021. For comparing GEMS and TROPOMI products, GEMS VCDs are averaged in  $0.5^\circ \times 0.5^\circ$  grids weighted by the overlapping area between pixels and grid boxes. For comparison, we used hourly GEMS data (FinalAlgorithmFlags = 0, cloud fraction < 0.4) at the TROPOMI overpass time in each region. TROPOMI L3 glyoxal data with a spatial resolution of  
265  $0.05^\circ \times 0.05^\circ$  are regridded into the same  $0.5^\circ \times 0.5^\circ$  grids for ~~the~~ comparison.

Figures [5a8a](#) and [5b8b](#) show GEMS and TROPOMI glyoxal VCDs averaged from August 2020 to July 2021 at 11:30–15:30 local time. We find good consistencies between the two products over the whole domain, with a correlation

coefficient of 0.63 and a regression slope of 1.26 (Figure 5d8d). Both products show high VCDs in the Indochinese Peninsula and populated cities such as Shanghai and Guangdong due to biogenic or anthropogenic emissions of VOCs. However, GEMS is slightly higher than TROPOMI in Northeast Asia. This discrepancy may be partly due to the elevated NO<sub>2</sub> concentration. Lerot et al. (2021) conducted an empirical correction for strong NO<sub>2</sub> absorption for TROPOMI, which decreased glyoxal concentrations as a function of NO<sub>2</sub> SCDs. The correction of GEMS glyoxal VCDs accounting for the strong absorption NO<sub>2</sub> needs to be developed as the current operational product (GEMS glyoxal V2.0) does not consider this effect.

In the west of the domain, the negative bias of GEMS VCDs compared to TROPOMI occurs due to the GEMS's high viewing zenith angle (Figure 5e8c). A similar negative bias is also found in formaldehyde retrieval (Lee et al., 2023 Preprint)2024). GEMS glyoxal VCDs are even negative in parts of the Indian Ocean, the area outside the dashed green line depicted in Figure 47, in which no clear reasons for this issue have been found yet. Excluding this region in our scatter increases the correlation coefficient to 0.71 between the two products (Figure 5e8e). We also find an excellent agreement (R=0.87) between the two products in Northeast Asia, defined as Domain 2 in Figure 47, which includes Eastern China and Korea (Figure 5f8f).

Figure 69 shows monthly mean VCDs of GEMS and TROPOMI averaged in six regions (Figure 47) from August 2020 to December 2022. Values are high in Cambodia and Myanmar, especially in spring, due to biomass burning influences, which are consistently captured by the two products with relatively high correlation coefficients (0.67–0.89). However, GEMS is somewhat inconsistent in regions located in Northeast Asia, such as Korea, North China Plain (NCP), and Yangtze River Delta (YRD), showing low correlation coefficients (0.16–0.40) with TROPOMI, mainly driven by too high GEMS values in winter. PositiveThe positive bias of GEMS in winter may be due to high NO<sub>2</sub> concentration, which is notable in NCP. Mean GEMS

~~To eliminate artifacts caused by NO<sub>2</sub> SCDs over NCP are  $1.57 \times 10^{16}$  molecules cm<sup>-2</sup> in June 2021 and  $2.74 \times 10^{16}$  molecules cm<sup>-2</sup> in December 2021. The relative differences of GEMS and TROPOMI ( $\frac{GEMS-TROPOMI}{TROPOMI}$ ) glyoxal VCDs in NCP are -5% and 167% in June 2021 and December 2021, respectively. If we empirically correct corrected glyoxal SCDs using the same linear regression equation derived from the TROPOMI glyoxal retrieval algorithm ( $-8.75 \times 10^{12} - 7.01 \times 10^{-3} \times NO_2 \text{ SCD}$ ; Lerot et al., 2021). The corrected GEMS VCDs are depicted in grey lines in Figure 9. Monthly averaged GEMS NO<sub>2</sub> SCDs V2.0 in 2021 are used to correct GEMS glyoxal SCDs for all years (2020, 2021, 2022). In NCP, where the NO<sub>2</sub> concentration is the highest, mean GEMS NO<sub>2</sub> SCDs are  $1.57 \times 10^{16}$  molecules cm<sup>-2</sup> in June 2021 and  $2.74 \times 10^{16}$  molecules cm<sup>-2</sup> in December 2021. The relative differences are -33% and 23% in June between GEMS and TROPOMI ( $\frac{GEMS-TROPOMI}{TROPOMI}$ ) glyoxal VCDs in NCP without applying NO<sub>2</sub> correction are -5% and 167% in June 2021 and December 2021, respectively. When the NO<sub>2</sub> correction is applied, the relative differences are -28% and 49% in June and December 2021, respectively. While the negative bias in the summer worsens to some extent, the positive bias in the winter~~

300 improves significantly. As a result, the monthly correlation coefficients improve drastically from 0.16–0.40 to 0.45–0.72 in the regions with high NO<sub>2</sub> concentrations, including Korea, NCP, and YRD.

The underestimation of GEMS VCDs compared to TROPOMI in the summer in Northeast Asia could be attributed to the polluted reference spectrum. ~~Most of the scan area from August to September 2020 was a nominal daily or full central scan (Figure 1 of Kwon et al., 2019). However, since October 2020, the scan area has changed to a full central or full western scan, decreasing the area for sampling radiance reference.~~ Although the simulated VCDs are averaged in the same area for the background correction, this does not fully compensate for the reduction in the differential slant column since GEOS-Chem underestimates glyoxal concentration (Bates and Jacob, 2019; ~~Silva et al., 2018~~; Chan Miller et al., 2017); ~~Silva et al., 2018~~). This could result in the low seasonal variation of GEMS VCDs, especially in the high latitudes, where the reference sector is somewhat polluted.

310 ~~Figure 7 demonstrates the sensitivity of retrieved glyoxal VCDs to the selection of reference spectrum depending on the scan schedules. During the in orbit test period (IOT), observations were frequently taken as a nominal daily scan, which covers 90–150° E, enabling us to obtain the reference spectrum over 120–150° E. Figure 7a illustrates glyoxal VCDs retrieved with the reference spectrum taken from the reference sector of 120–150° E in August 2020. Figure 7b shows the same retrieved glyoxal VCDs but with the reference spectrum averaged over 120–133° E, which is the narrow reference sector limited by the full western scan, frequently conducted after the IOT. Values in Figure 7b are about 22% lower than those in Figure 7a, possibly due to the effect of local pollution on the reference spectrum. The largest discrepancy occurs in 28–40° N, including Korea, NCP, and YRD (Figure 7c). In Figure 5c, the largest discrepancy depending on the reference sector occurs in 28–40° N, including Korea, NCP, and YRD.~~ Obtaining the reference spectrum from the clean region is very crucial for the GEMS glyoxal product.

## 320 **4.5 Comparison with MAX-DOAS observations**

This section evaluates GEMS VCDs with ground-based Multi-Axis Differential Optical Absorption Spectroscopy (MAX-DOAS) observations (Lerot et al., 2021) at Chiba, Kasuga, Fukue, Phimai, Pantnagar, Haldwani, Seoul, and Xianghe (Figure 47) from August 2020 to December 2021. MAX-DOAS data at Xianghe are operated by BIRA-IASB (Hendrick et al., 2014), and data for the other six stations are operated by CERES (Irie et al., 2011). Each institution uses different ~~fitting intervals and profile retrieval algorithms-instruments and retrieval algorithms (fitting intervals, absorption cross-sections, etc.), leading to the possibility that instruments from each institution contain distinct systematic biases. Acknowledging this limitation, Lerot et al. (2021) compared TROPOMI glyoxal VCDs with MAX-DOAS glyoxal VCDs from different institutions. A mean bias of MAX-DOAS glyoxal VCDs from BIRA-IASB ( $-0.8 \times 10^{14}$  molecules cm<sup>-2</sup>) is within a range of mean bias of MAX-DOAS glyoxal VCDs from CERES ( $-3.5 \times 10^{14}$ – $0.1 \times 10^{14}$ ) when compared with TROPOMI glyoxal VCDs. It is uncertain whether there are significant systematic biases between the instruments. Instead, inconsistent biases~~

330

across the stations could result from the different profiles and aerosol concentrations. The data from Pantnagar and Haldwani were merged and shown in the same subplot, considering their geographical proximity and the lack of temporal overlap; measurements in Pantnagar were made until January 2021, and those in Haldwani were from June 2021. We filtered out MAX-DOAS observations with random uncertainty higher than 30%, primarily from the Pantnagar site. We averaged GEMS VCD pixels within  $0.72^\circ$  from the MAX-DOAS stations for comparison, considering the spatial resolution of GEMS glyoxal data. All the data are hourly and coherently sampled at the same local time. In addition, GEMS VCDs compared with MAX-DOAS VCDs are the values without applying  $\text{NO}_2$  correction described in Sect. 4.

Figure [810](#) compares monthly mean GEMS and MAX-DOAS glyoxal VCDs. Both show a reasonable agreement in Northeast Asia (Chiba, Kasuga, Fukue, Seoul, and Xianghe) despite some discrepancies of GEMS being low in summer and high in winter, as shown in the comparison with TROPOMI. In Phimai, GEMS VCDs are slightly lower than MAX-DOAS VCDs but show similar seasonal variations. At the Pantnagar and Haldwani sites, uncertainties are high due to the few MAX-DOAS observations and possible aerosol contamination (Lerot et al., 2021). Underestimation of GEMS VCDs in India is also found in the formaldehyde product, which could be attributed to the longer light path at high viewing zenith angles (Lee et al., [2023-Preprint](#)2024).

Figure [911](#) compares hourly mean GEMS and MAX-DOAS glyoxal VCDs. We find a good agreement between the two datasets regarding glyoxal diurnal variations in Japan (Chiba, Kasuga, and Fukue). Chiba is located near Tokyo and shows elevated concentrations compared to rural sites like Kasuga and Fukue. GEMS underestimates VCDs at the Phimai, Pantnagar, and Haldwani sites, located west of other sites. In Seoul, GEMS and MAX-DOAS VCDs are similar until 14:00 local time and diverge afterward. The continuous increase in the ~~MASMAX~~-DOAS observations is not reasonable, though further validation is necessary. GEMS and MAX-DOAS VCDs at Xianghe are consistent except at low solar zenith angles, as fewer samples are available.

## **56 Conclusion and discussions**

This study presents the ~~inaugural~~first retrieval of glyoxal columns from ~~the~~a geostationary satellite. To reduce the uncertainty associated with SCD retrieval, we selected optimal settings for the spectral fitting based on sensitivity tests involving the reference spectrum and fitting window. The retrieved SCDs are converted to VCDs using ~~AMFAMFs~~ derived from high-resolution GEOS-Chem simulations. The background correction is the final process ~~to add of adding~~ column amounts over the reference sector. The capability of GEMS to observe hourly glyoxal VCDs offers unparalleled temporal resolution, enriching our understanding of VOC emissions and transport.

We compared the retrieved glyoxal VCDs with other satellite and ground-based measurements. GEMS and TROPOMI VCDs generally show similar spatial distribution; however, GEMS VCDs tend to be higher in the north-eastern domain and lower in the south-western domain than TROPOMI VCDs. While monthly variations of GEMS VCDs correlate

well with those of TROPOMI and MAX-DOAS VCDs in the Indochinese peninsula regions, variations differ in Northeast Asia. The biases of GEMS may result from the interference with high NO<sub>2</sub> concentration, polluted reference spectrum, and high viewing zenith angle.

365 To address the overestimation in the high NO<sub>2</sub> regions, the wavelength dependency of NO<sub>2</sub> absorption must be considered. Correction of the glyoxal column with NO<sub>2</sub> concentration could improve the consistency of GEMS VCDs with other measurements regarding spatial distribution and temporal variation. This is because the overestimation becomes more pronounced in winter when NO<sub>2</sub> concentration is higher. However, subtracting the glyoxal column as a function of NO<sub>2</sub> concentration could exacerbate the underestimation of GEMS glyoxal VCDs in summer in Northeast Asia. Therefore,  
370 simultaneous work must be performed to resolve the polluted reference spectrum issue. We could consider methods such as filtering pixels representing high glyoxal concentrations simulated from the CTM over the reference sector or utilizing synthetic radiances from the RTM.

The limited field of regard of GEMS poses significant challenges in finding a clean reference sector. While background concentrations in the reference sector are corrected from the simulated concentrations, this is insufficient to  
375 resolve bias in GEMS VCDs because the CTM used for background correction underestimates glyoxal VCDs. Enhancing the fidelity of CTMs, particularly in terms of emission and oxidative chemistry of precursor VOCs, is required to mitigate bias in GEMS VCDs across monthly and diurnal variations. While the availability of in-situ glyoxal measurements for reference purposes is limited, the Airborne and Satellite Investigation of Asian Air Quality (ASIA-AQ) campaign presents a promising opportunity. This initiative will comprehensively evaluate observed and simulated glyoxal columns and enhance our  
380 understanding of atmospheric processes at scales finer than those resolvable by satellite pixels.

### **Data availability.**

385 The GEMS Level 1C data are available on request from the National Institute of Environmental Research (NIER) –  
Environmental Satellite Center (ESC). The GEMS Level 2 products are available at <https://nesc.nier.go.kr/ko/html/index.do>  
(last access: 28 February 2024). Access to TROPOMI glyoxal tropospheric column data is possible via the GLYRETRO  
website at <https://glyretro.aeronomie.be/index.php/data-menu-item/request-data-test/new-data> (last access: 28 February 2024)  
(Lerot et al., 2021).

### 390 **Author contributions.**

ESH, RJP, and HAK designed the study, carried out the analyses, and wrote the manuscript. GTL, SDL, and SS participated  
in the algorithm development. DWL and HH supported the GEMS instrument. CL and IDS provided the TROPOMI glyoxal  
product. FH, HI carried out the MAX-DOAS measurement.

### 395 **Competing interests.**

The contact author has declared that none of the authors has any competing interests.

### **Special issue statement.**

400 This article is part of the special issue “GEMS: first year in operation (AMT/ACP inter-journal SI)”. It is not associated with  
a conference.

### **Acknowledgements.**

The authors thank the GEMS science team and the Environment Satellite Center (ESC) of National Institute of  
Environmental Research (NIER) for supporting the GEMS glyoxal retrieval algorithm development.  
405

### **Financial support.**

This research was supported by a grant from the Nation Institute of Environmental Research (NIER), funded by the Korea  
Ministry of Environment (MOE) of the Republic of Korea (NIER-2023-04-02-050).

### **References**

410 Alvarado, L. M. A., Richter, A., Vrekoussis, M., Wittrock, F., Hilboll, A., Schreier, S. F., and Burrows, J. P.: An improved  
glyoxal retrieval from OMI measurements, *Atmos Meas Tech*, 7, 4133–4150, <https://doi.org/10.5194/amt-7-4133-2014>,  
2014.

- Alvarado, L. M. A., Richter, A., Vrekoussis, M., Hilboll, A., Kalisz Hedegaard, A. B., Schneising, O., and Burrows, J. P.: Unexpected long-range transport of glyoxal and formaldehyde observed from the Copernicus Sentinel-5 Precursor satellite during the 2018 Canadian wildfires, *Atmos Chem Phys*, 20, 2057–2072, <https://doi.org/10.5194/acp-20-2057-2020>, 2020.
- 415 Bates, K. H. and Jacob, D. J.: A new model mechanism for atmospheric oxidation of isoprene: Global effects on oxidants, nitrogen oxides, organic products, and secondary organic aerosol, *Atmos Chem Phys*, 19, 9613–9640, <https://doi.org/10.5194/acp-19-9613-2019>, 2019.
- Bey, I., Jacob, D. J., Yantosca, R. M., Logan, J. A., Field, B. D., Fiore, A. M., Li, Q., Liu, H. Y., Mickley, L. J., and Schultz, M. G.: Global modeling of tropospheric chemistry with assimilated meteorology: Model description and evaluation, *Journal of Geophysical Research Atmospheres*, 106, 23073–23095, <https://doi.org/10.1029/2001JD000807>, 2001.
- 420 [Boersma, K. F., Eskes, H. J., and Brinksma, E. J.: Error analysis for tropospheric NO<sub>2</sub> retrieval from space, \*Journal of Geophysical Research: Atmospheres\*, 109, <https://doi.org/10.1029/2003jd003962>, 2004.](https://doi.org/10.1029/2003jd003962)
- Cao, H., Fu, T. M., Zhang, L., Henze, D. K., Miller, C. C., Lerot, C., Abad, G. G., De Smedt, I., Zhang, Q., Van Roozendael, M., Hendrick, F., Chance, K., Li, J., Zheng, J., and Zhao, Y.: Adjoint inversion of Chinese non-methane volatile organic compound emissions using space-based observations of formaldehyde and glyoxal, *Atmos Chem Phys*, 18, 15017–15046, <https://doi.org/10.5194/acp-18-15017-2018>, 2018.
- 425 Chan Miller, C., Gonzalez Abad, G., Wang, H., Liu, X., Kurosu, T., Jacob, D. J., and Chance, K.: Glyoxal retrieval from the ozone monitoring instrument, *Atmos Meas Tech*, 7, 3891–3907, <https://doi.org/10.5194/amt-7-3891-2014>, 2014.
- 430 Chan Miller, C., Jacob, D., González Abad, G., and Chance, K.: Hotspot of glyoxal over the Pearl River delta seen from the OMI satellite instrument: Implications for emissions of aromatic hydrocarbons, *Atmos Chem Phys*, 16, 4631–4639, <https://doi.org/10.5194/acp-16-4631-2016>, 2016.
- Chan Miller, C., Jacob, D. J., Marais, E. A., Yu, K., Travis, K. R., Kim, P. S., Fisher, J. A., Zhu, L., Wolfe, G. M., Hanisco, T. F., Keutsch, F. N., Kaiser, J., Min, K. E., Brown, S. S., Washenfelder, R. A., González Abad, G., and Chance, K.: Glyoxal yield from isoprene oxidation and relation to formaldehyde: Chemical mechanism, constraints from SENEX aircraft observations, and interpretation of OMI satellite data, *Atmos Chem Phys*, 17, 8725–8738, <https://doi.org/10.5194/acp-17-8725-2017>, 2017.
- 435 Chance, K. and Kurucz, R. L.: An improved high-resolution solar reference spectrum for earth’s atmosphere measurements in the ultraviolet, visible, and near infrared, *J Quant Spectrosc Radiat Transf*, 111, 1289–1295, 2010.
- 440 Choi, J., Henze, D. K., Cao, H., Nowlan, C. R., González Abad, G., Kwon, H. A., Lee, H. M., Oak, Y. J., Park, R. J., Bates, K. H., Maasackers, J. D., Wisthaler, A., and Weinheimer, A. J.: An Inversion Framework for Optimizing Non-Methane VOC Emissions Using Remote Sensing and Airborne Observations in Northeast Asia During the KORUS-AQ Field Campaign, *Journal of Geophysical Research: Atmospheres*, 127, <https://doi.org/10.1029/2021JD035844>, 2022.
- 445 Digangi, J. P., Henry, S. B., Kammrath, A., Boyle, E. S., Kaser, L., Schnitzhofer, R., Graus, M., Turnipseed, A., Weber, R. J., Hornbrook, R. S., Cantrell, C. A., Maudlin, R. L., Kim, S., Nakashima, Y., Wolfe, G. M., Kajii, Y., Apel, E. C.,



- Goldstein, A. H., Guenther, A., Karl, T., Hansel, A., and Keutsch, F. N.: Observations of glyoxal and formaldehyde as metrics for the anthropogenic impact on rural photochemistry, *Atmos Chem Phys*, 12, 9529–9543, <https://doi.org/10.5194/acp-12-9529-2012>, 2012.
- 450 Dufour, G., Wittrock, F., Camredon, M., Beekmann, M., Richter, A., Aumont, B., and Burrows, J. P.: Atmospheric Chemistry and Physics SCIAMACHY formaldehyde observations: constraint for isoprene emission estimates over Europe?, *Atmos. Chem. Phys.*, 1647–1664 pp., 2009.
- Finkenzeller, H. and Volkamer, R.: O<sub>2</sub>–2 CIA in the gas phase: Cross-section of weak bands, and continuum absorption between 297–500 nm, *J Quant Spectrosc Radiat Transf*, 108063, 2022.
- 455 Fu, T. M., Jacob, D. J., Wittrock, F., Burrows, J. P., Vrekoussis, M., and Henze, D. K.: Global budgets of atmospheric glyoxal and methylglyoxal, and implications for formation of secondary organic aerosols, *Journal of Geophysical Research Atmospheres*, 113, <https://doi.org/10.1029/2007JD009505>, 2008.
- Gordon, I. E., Rothman, L. S., Hargreaves, R. J., Hashemi, R., Karlovets, E. V., Skinner, F. M., Conway, E. K., Hill, C., Kochanov, R. V., Tan, Y., Wcisło, P., Finenko, A. A., Nelson, K., Bernath, P. F., Birk, M., Boudon, V., Campargue, A., Chance, K. V., Coustenis, A., Drouin, B. J., Flaud, J. M., Gamache, R. R., Hodges, J. T., Jacquemart, D., Mlawer, E. J., 460 Nikitin, A. V., Perevalov, V. I., Rotger, M., Tennyson, J., Toon, G. C., Tran, H., Tyuterev, V. G., Adkins, E. M., Baker, A., Barbe, A., Canè, E., Császár, A. G., Dudaryonok, A., Egorov, O., Fleisher, A. J., Fleurbaey, H., Foltynowicz, A., Furtenbacher, T., Harrison, J. J., Hartmann, J. M., Horneman, V. M., Huang, X., Karman, T., Karns, J., Kassi, S., Kleiner, I., Kofman, V., Kwabia-Tchana, F., Lavrentieva, N. N., Lee, T. J., Long, D. A., Lukashetskaya, A. A., Lyulin, O. M., Makhnev, V. Y., Matt, W., Massie, S. T., Melosso, M., Mikhailenko, S. N., Mondelain, D., Müller, H. S. P., Naumenko, O. 465 V., Perrin, A., Polyansky, O. L., Raddaoui, E., Raston, P. L., Reed, Z. D., Rey, M., Richard, C., Tóbiás, R., Sadiék, I., Schwenke, D. W., Starikova, E., Sung, K., Tamassia, F., Tashkun, S. A., Vander Auwera, J., Vasilenko, I. A., Viganin, A. A., Villanueva, G. L., Vispoel, B., Wagner, G., Yachmenev, A., and Yurchenko, S. N.: The HITRAN2020 molecular spectroscopic database, *J Quant Spectrosc Radiat Transf*, 277, <https://doi.org/10.1016/j.jqsrt.2021.107949>, 2022.
- 470 Guenther, A. B., Jiang, X., Heald, C. L., Sakulyanontvittaya, T., Duhl, T., Emmons, L. K., and Wang, X.: The model of emissions of gases and aerosols from nature version 2.1 (MEGAN2.1): An extended and updated framework for modeling biogenic emissions, *Geosci Model Dev*, 5, 1471–1492, <https://doi.org/10.5194/gmd-5-1471-2012>, 2012.
- Hendrick, F., Clémer, K., Wang, P., De Mazière, M., Fayt, C., Gielen, C., Hermans, C., Ma, J. Z., Pinardi, G., Stavrakou, T., Vlemmix, T., and Van Roozendaal, M.: Four years of ground-based MAX-DOAS observations of HONO and NO<sub>2</sub> in the Beijing area, *Atmos Chem Phys*, 14, 765–781, <https://doi.org/10.5194/acp-14-765-2014>, 2014.
- 475 Irie, H., Takashima, H., Kanaya, Y., Boersma, K. F., Gast, L., Wittrock, F., Brunner, D., Zhou, Y., and Van Roozendaal, M.: Eight-component retrievals from ground-based MAX-DOAS observations, *Atmos Meas Tech*, 4, 1027–1044, <https://doi.org/10.5194/amt-4-1027-2011>, 2011.

- Kim, J., Jeong, U., Ahn, M. H., Kim, J. H., Park, R. J., Lee, H., Song, C. H., Choi, Y. S., Lee, K. H., Yoo, J. M., Jeong, M. J., Park, S. K., Lee, K. M., Song, C. K., Kim, S. W., Kim, Y. J., Kim, S. W., Kim, M., Go, S., Liu, X., Chance, K., Miller, C. C., Al-Saadi, J., Veihelmann, B., Bhartia, P. K., Torres, O., Abad, G. G., Haffner, D. P., Ko, D. H., Lee, S. H., Woo, J. H., Chong, H., Park, S. S., Nicks, D., Choi, W. J., Moon, K. J., Cho, A., Yoon, J., Kim, S. kyun, Hong, H., Lee, K., Lee, H., Lee, S., Choi, M., Veefkind, P., Levelt, P. F., Edwards, D. P., Kang, M., Eo, M., Bak, J., Baek, K., Kwon, H. A., Yang, J., Park, J., Han, K. M., Kim, B. R., Shin, H. W., Choi, H., Lee, E., Chong, J., Cha, Y., Koo, J. H., Irie, H., Hayashida, S., Kasai, Y., Kanaya, Y., Liu, C., Lin, J., Crawford, J. H., Carmichael, G. R., Newchurch, M. J., Lefer, B. L., Herman, J. R., Swap, R. J., Lau, A. K. H., Kurosu, T. P., Jaross, G., Ahlers, B., Dobber, M., McElroy, C. T., and Choi, Y.: New era of air quality monitoring from space: Geostationary environment monitoring spectrometer (GEMS), *Bull Am Meteorol Soc*, 101, E1–E22, <https://doi.org/10.1175/BAMS-D-18-0013.1>, 2020.
- Kleipool, Q.: OMI/Aura Surface Reflectance Climatology L3 Global Gridded 0.5 degree x 0.5 degree V3, 2010.
- [Kluge, F., Huneke, T., Lerot, C., Rosanka, S., Rotermund, M. K., Taraborrelli, D., Weyland, B., and Pfeilsticker, K.: Airborne glyoxal measurements in the marine and continental atmosphere: Comparison with TROPOMI observations and EMAC simulations. \*Atmos Chem Phys\*, 23, 1369–1401, <https://doi.org/10.5194/acp-23-1369-2023>, 2023.](#)
- Kwon, H. A., Park, R. J., Abad, G. G., Chance, K., Kurosu, T. P., Kim, J., De Smedt, I., Van Roozendaal, M., Peters, E., and Burrows, J.: Description of a formaldehyde retrieval algorithm for the Geostationary Environment Monitoring Spectrometer (GEMS), *Atmos Meas Tech*, 12, 3551–3571, <https://doi.org/10.5194/amt-12-3551-2019>, 2019.
- Kwon, H. A., Park, R. J., Oak, Y. J., Nowlan, C. R., Janz, S. J., Kowalewski, M. G., Fried, A., Walega, J., Bates, K. H., Choi, J., Blake, D. R., Wisthaler, A., and Woo, J. H.: Top-down estimates of anthropogenic VOC emissions in South Korea using formaldehyde vertical column densities from aircraft during the KORUS-AQ campaign, *Elementa*, 9, <https://doi.org/10.1525/elementa.2021.00109>, 2021.
- Lee, G. T., Park, R. J., Kwon, H.-A., Ha, E. S., Lee, S. D., Shin, S., Ahn, M.-H., Kang, M., Choi, Y.-S., Kim, G., Lee, D.-W., Kim, D.-R., Hong, H., Langerock, B., Vigouroux, C., Lerot, C., Hendrick, F., Pinaridi, G., De Smedt, I., [Van Roozendaal, M., Wang, P., Chong, H., Cho, Y., and Kim, J.: First evaluation of the GEMS formaldehyde retrieval algorithm product against TROPOMI and ground-based column measurements during the in-orbit test period, \*EGUsphere \[preprint\]\*, \*Atmos Chem Phys\*, 24, 4733–4749, <https://doi.org/10.5194/egusphere-2023-1918>, \[2023acp-24-4733-2024\]\(https://doi.org/10.5194/acp-24-4733-2024\), 2024.](#)
- Lerot, C., Stavroukou, T., De Smedt, I., Müller, J. F., and Van Roozendaal, M.: Glyoxal vertical columns from GOME-2 backscattered light measurements and comparisons with a global model, *Atmos Chem Phys*, 10, 12059–12072, <https://doi.org/10.5194/acp-10-12059-2010>, 2010.
- Lerot, C., Hendrick, F., Van Roozendaal, M., Alvarado, L. M. A., Richter, A., De Smedt, I., Theys, N., Vlietinck, J., Yu, H., Van Gent, J., Stavroukou, T., Müller, J. F., Valks, P., Loyola, D., Irie, H., Kumar, V., Wagner, T., Schreier, S. F., Sinha, V., Wang, T., Wang, P., and Retscher, C.: Glyoxal tropospheric column retrievals from TROPOMI -multi-satellite

- 510 intercomparison and ground-based validation, *Atmos Meas Tech*, 14, 7775–7807, <https://doi.org/10.5194/amt-14-7775-2021>, 2021.
- Li, J., Zhang, M., Tang, G., Wu, F., Alvarado, L. M. A., Vrekoussis, M., Richter, A., and Burrows, J. P.: Investigating missing sources of glyoxal over China using a regional air quality model (RAMS-CMAQ), *J Environ Sci (China)*, 71, 108–118, <https://doi.org/10.1016/j.jes.2018.04.021>, 2018.
- 515 Mason, J. D., Cone, M. T., and Fry, E. S.: Ultraviolet (250–550 nm) absorption spectrum of pure water, *Appl Opt*, 55, 7163, <https://doi.org/10.1364/ao.55.007163>, 2016.
- Palmer, P. I., Jacob, D. J., Chance, K., Martin, R. V., Spurr, R. J. D., Kurosu, T. P., Bey, I., Yantosca, R., Fiore, A., and Li, Q.: Air mass factor formulation for spectroscopic measurements from satellites: Application to formaldehyde retrievals from the Global Ozone Monitoring Experiment, *Journal of Geophysical Research Atmospheres*, 106, 14539–14550, <https://doi.org/10.1029/2000JD900772>, 2001.
- 520 [Rodgers C. D.: Inverse Methods for Atmospheric Sounding, Theory and Practice. World Scientific Publishing, Singapore-New Jersey-London-Hong Kong, 2000.](#)
- Serdyuchenko, A., Gorshelev, V., Weber, M., Chehade, W., and Burrows, J. P.: High spectral resolution ozone absorption cross-sections—Part 2: Temperature dependence, *Atmos Meas Tech*, 7, 625–636, 2014.
- 525 Silva, S. J., Heald, C. L., and Li, M.: Space-Based Constraints on Terrestrial Glyoxal Production, *Journal of Geophysical Research: Atmospheres*, 123, 13,583–13,594, <https://doi.org/10.1029/2018JD029311>, 2018.
- Sinreich, R., Coburn, S., Dix, B., and Volkamer, R.: Ship-based detection of glyoxal over the remote tropical Pacific Ocean, *Atmos Chem Phys*, 10, 11359–11371, <https://doi.org/10.5194/acp-10-11359-2010>, 2010.
- 530 [De Smedt, I., Theys, N., Yu, H., Danckaert, T., Lerot, C., Compennolle, S., Van Roozendael, M., Richter, A., Hilboll, A., Peters, E., Pedergnana, M., Loyola, D., Beirle, S., Wagner, T., Eskes, H., Van Geffen, J., Folkert Boersma, K., and Veefkind, P.: Algorithm theoretical baseline for formaldehyde retrievals from S5P TROPOMI and from the QA4ECV project, \*Atmos Meas Tech\*, 11, 2395–2426, <https://doi.org/10.5194/amt-11-2395-2018>, 2018.](#)
- Spurr, R. J. D.: VLIDORT: A linearized pseudo-spherical vector discrete ordinate radiative transfer code for forward model and retrieval studies in multilayer multiple scattering media, *J Quant Spectrosc Radiat Transf*, 102, 316–342, <https://doi.org/10.1016/j.jqsrt.2006.05.005>, 2006.
- 535 Vandaele, A. C., Hermans, C., Simon, P. C., Carleer, M., Colin, R., Fally, S., Merienne, M.-F., Jenouvrier, A., and Coquart, B.: Measurements of the NO<sub>2</sub> absorption cross-section from 42 000 cm<sup>-1</sup> to 10 000 cm<sup>-1</sup> (238–1000 nm) at 220 K and 294 K, *J Quant Spectrosc Radiat Transf*, 59, 171–184, 1998.
- Volkamer, R., Spietz, P., Burrows, J., and Platt, U.: High-resolution absorption cross-section of glyoxal in the UV-vis and IR spectral ranges, *J Photochem Photobiol A Chem*, 172, 35–46, <https://doi.org/10.1016/j.jphotochem.2004.11.011>, 2005.
- 540 Volkamer, R., Barnes, I., Platt, U., Molina, L. T., and Molina, M. J.: Remote Sensing of Glyoxal by Differential Optical Absorption Spectroscopy (DOAS): Advancements in Simulation Chamber and Field Experiments, in: *Environmental*

Simulation Chambers: Application to Atmospheric Chemical Processes. Nato Science Series: IV: Earth and Environmental Science, vol. 62, edited by: Barnes, I. and Rudzinski, K. J., Springer, Dordrecht, 2006.

545 Vrekoussis, M., Wittrock, F., Richter, A., and Burrows, J. P.: Atmospheric Chemistry and Physics Temporal and spatial variability of glyoxal as observed from space, *Atmos. Chem. Phys.*, 4485–4504 pp., 2009.

Vrekoussis, M., Wittrock, F., Richter, A., and Burrows, J. P.: GOME-2 observations of oxygenated VOCs: What can we learn from the ratio glyoxal to formaldehyde on a global scale?, *Atmos Chem Phys*, 10, 10145–10160, <https://doi.org/10.5194/acp-10-10145-2010>, 2010.

550 Wang, Y. X., McElroy, M. B., Jacob, D. J., and Yantosca, R. M.: A nested grid formulation for chemical transport over Asia: Applications to CO, *Journal of Geophysical Research D: Atmospheres*, 109, 1–20, <https://doi.org/10.1029/2004JD005237>, 2004.

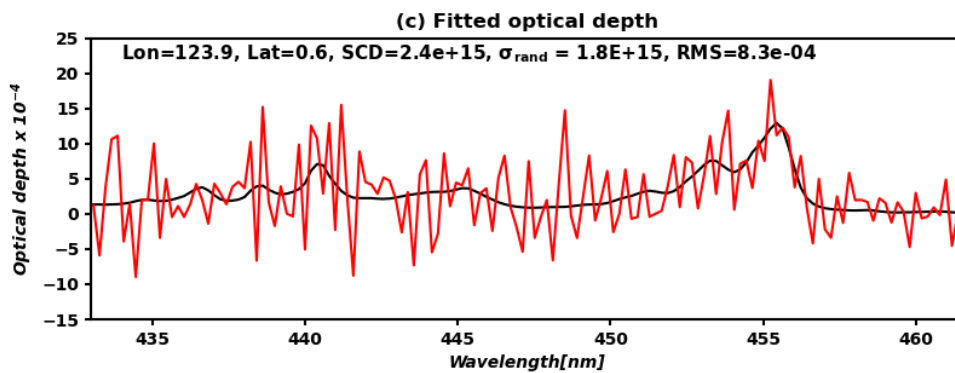
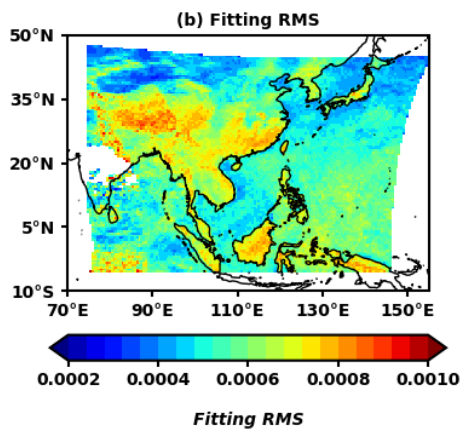
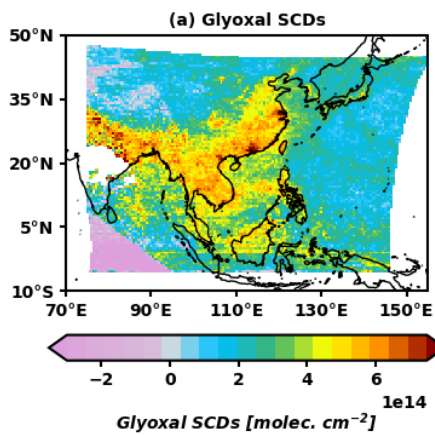
Van Der Werf, G. R., Randerson, J. T., Giglio, L., Collatz, G. J., Mu, M., Kasibhatla, P. S., Morton, D. C., Defries, R. S., Jin, Y., and Van Leeuwen, T. T.: Global fire emissions and the contribution of deforestation, savanna, forest, agricultural, and peat fires (1997-2009), *Atmos Chem Phys*, 10, 11707–11735, <https://doi.org/10.5194/acp-10-11707-2010>, 2010.

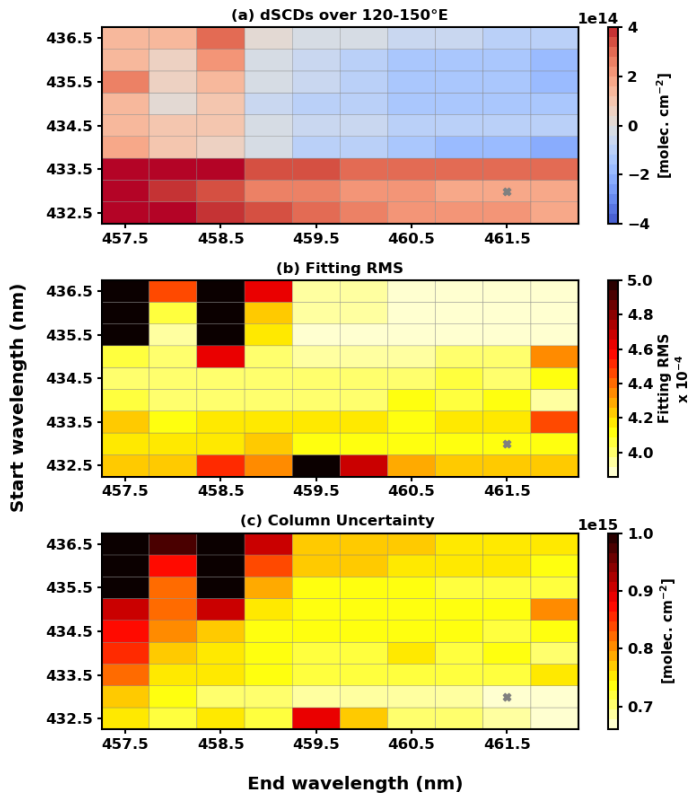
Wittrock, F.: The retrieval of oxygenated volatile organic compounds by remote sensing techniques, PhD Thesis, 2006.

Wittrock, F., Richter, A., Oetjen, H., Burrows, J. P., Kanakidou, M., Myriokefalitakis, S., Volkamer, R., Beirle, S., Platt, U., and Wagner, T.: Simultaneous global observations of glyoxal and formaldehyde from space, *Geophys Res Lett*, 33, <https://doi.org/10.1029/2006GL026310>, 2006.

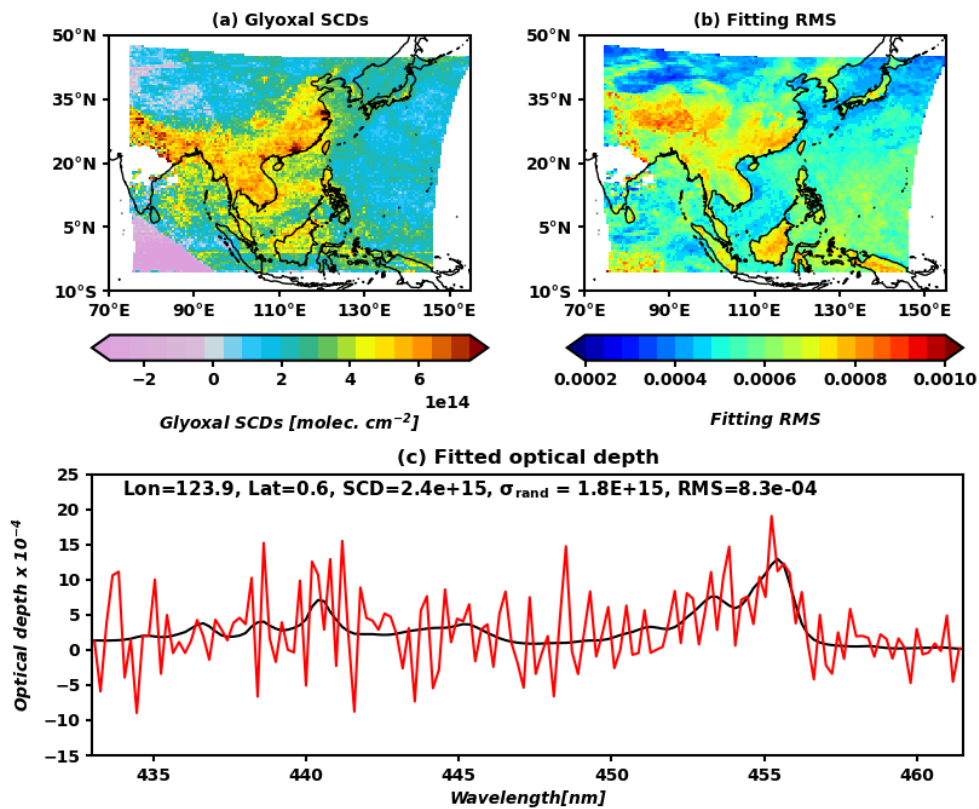
560 Woo, J. H.: ~~KORUS emissions: A comprehensive Asian emissions information in support of the NASA/NIER KORUS AQ mission, n.d.~~, Kim, Y., Kim, H. K., Choi, K. C., Eum, J. H., Lee, J. B., Lim, J. H., Kim, J., and Seong, M.: Development of the CREATE inventory in support of integrated climate and air quality modeling for Asia, *Sustainability (Switzerland)*, 12, <https://doi.org/10.3390/SU12197930>, 2020.

|565

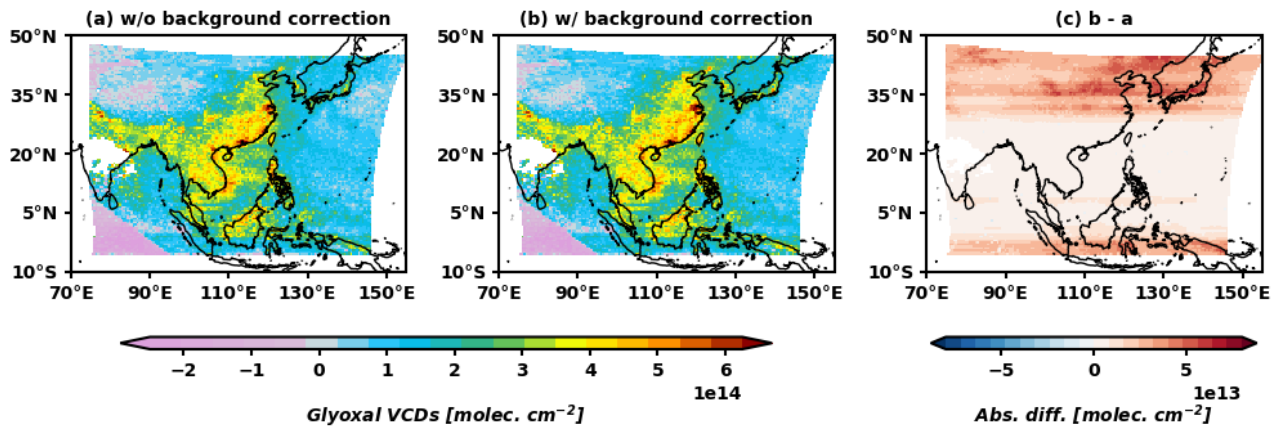




570 **Figure 1.** Metrics used to select an optimal fitting window. Panel a shows dSCDs averaged over 120–150° E, and panels b and c show fitting RMS and column uncertainty averaged over the entire domain. Values are calculated from the retrieval at 04:45 UTC on 17 March 2021.

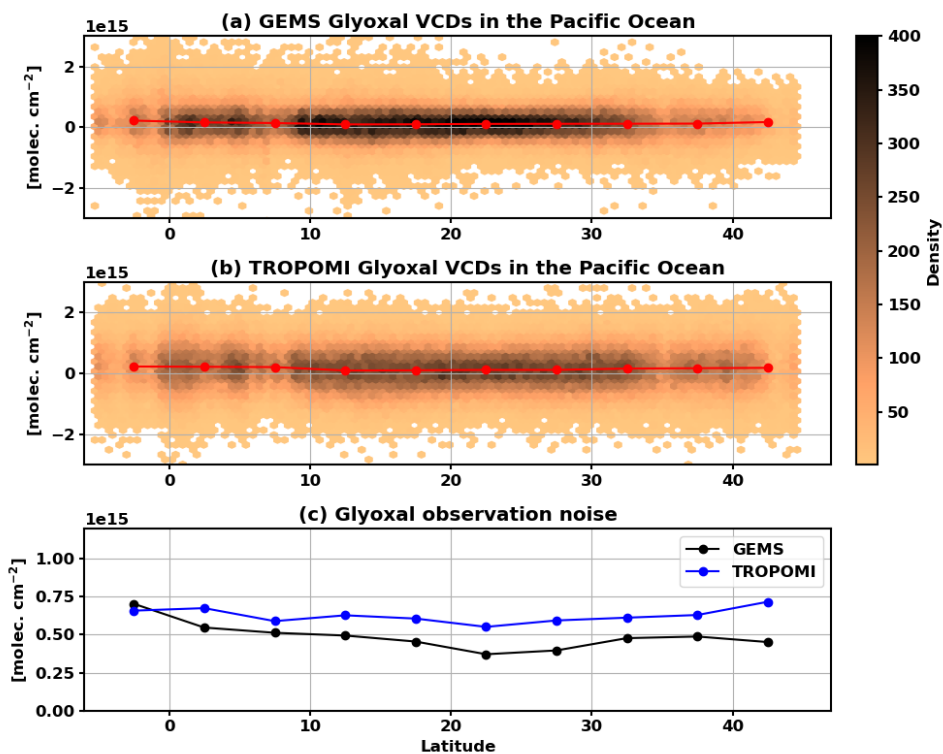


575 **Figure 2.** (a) GEMS glyoxal SCDs and (b) the root-mean-square values offrom the spectral fittingfit residuals averaged for 02:45–06:45 UTC in August 2020. (c) Fitted optical depth (black line) and the sum of optical depth and fitting residual (red line).



580 Figure 23. GEMS glyoxal VCDs retrieved (a) without background correction and (b) with background correction for 02:45–06:45 UTC in August 2020. (c) The absolute difference between (a) and (b).





585 Figure 34. (a) GEMS and (b) TROPOMI glyoxal VCDs in the ocean over 130–146° E on 3 August 2020. We filtered out pixels over  
 land with cloud cover (cloud fraction > 0.4). ~~The hexagons filled with colormap indicate~~The hexagonal heatmap indicates  
 the density of all data, and the red line indicate the data binned in 5° latitude bands. (c) The standard deviation of the binned data for  
 GEMS and TROPOMI.

590

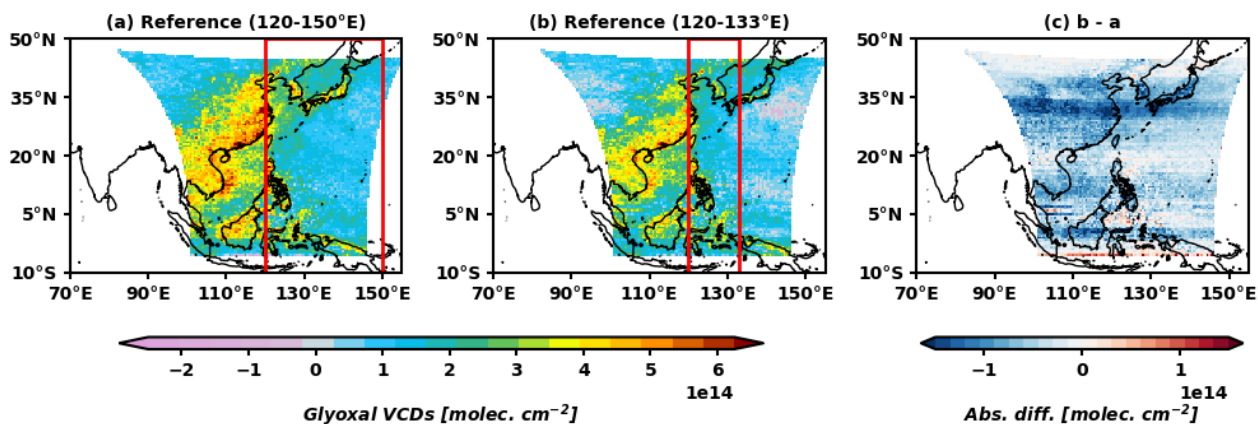


Figure 5. GEMS glyoxal VCDs averaged for the observations taken as Nominal daily scan for 02:45–06:45 UTC in August 2020. Panel a shows the VCDs retrieved with the reference sector of 120–133° E, and panel b shows those of 120–150° E. The red boxes in panel a and b indicate the reference sector used to retrieve each glyoxal VCDs. (c) The absolute difference between panel a and

595 b.

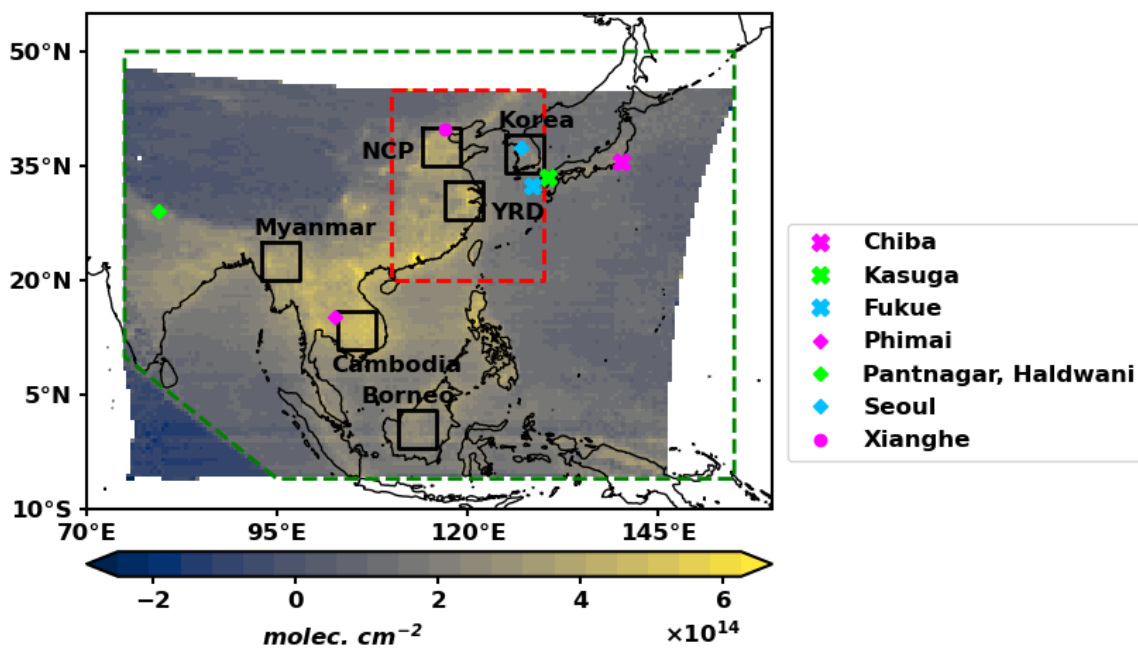
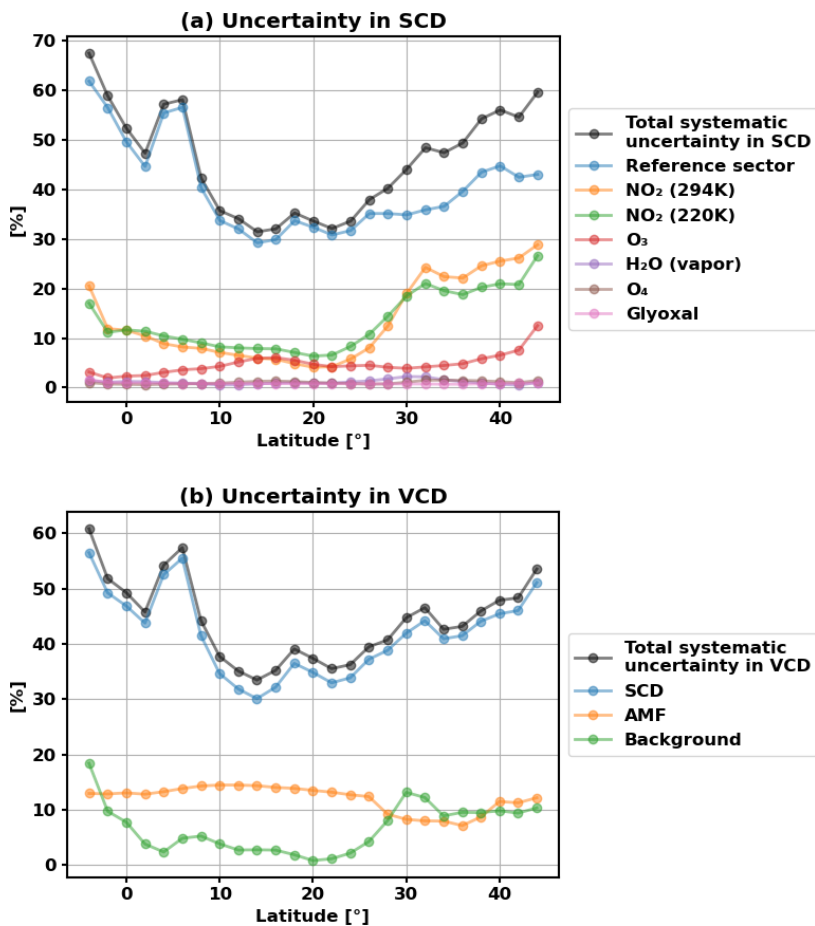


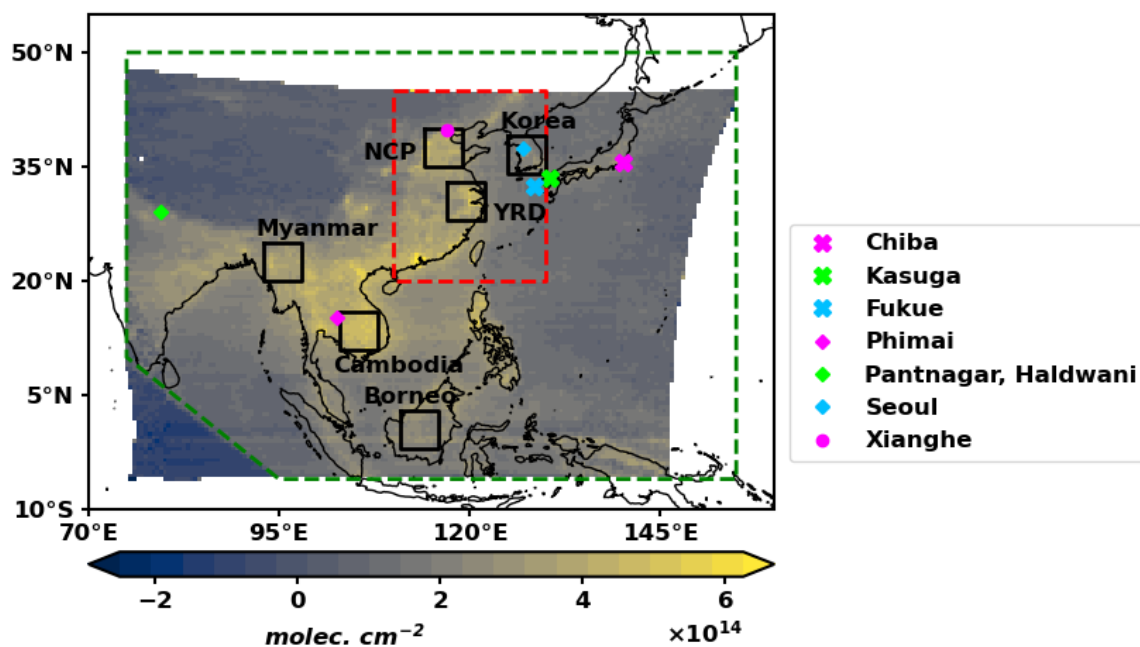
Figure 4.





**Figure 6. (a) The systematic uncertainty in SCD averaged at every 2 degrees latitude relative to glyoxal SCD. The total systematic uncertainty in SCD is indicated by the black line, and the contributions from each uncertainty source are indicated by the colored lines. (b) The systematic uncertainty in VCD averaged relative to glyoxal VCD. The total systematic uncertainty in VCD is indicated by the black line, and the contributions from SCD, AMF, and background correction are indicated by the colored lines.**

605

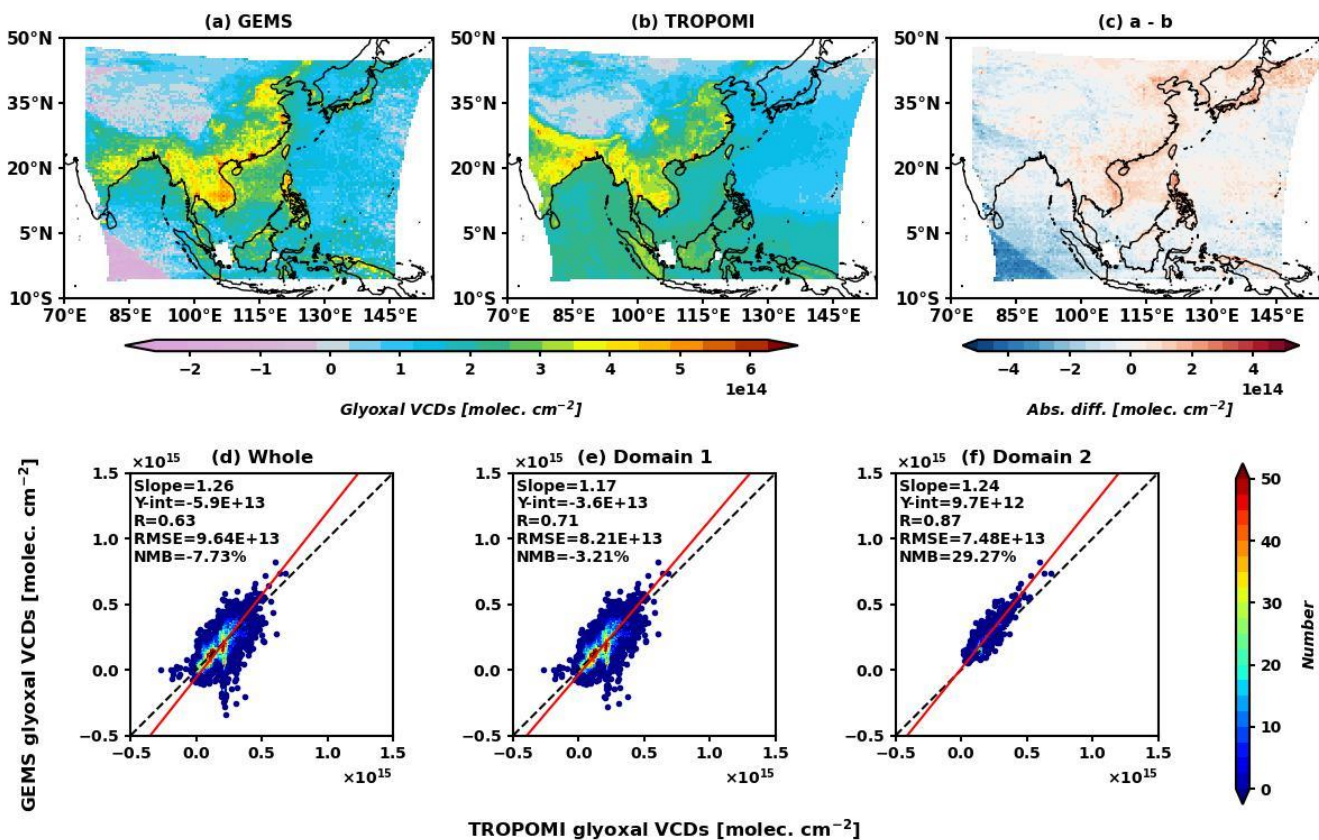


610

**Figure 7.** The green dashed line indicates outlines the area defined as Domain 1, and the red dashed line indicates outlines the area defined as Domain 2 (20–45° N, 110–130° E) in Figure 5.8. Domain 1 encompasses the area within the green dashed lines, including Domain 2. The black boxes indicate areas where glyoxal VCDs are averaged in Figure 69. Markers indicate the locations of the MAX-DOAS stations in Figure 810 and Figure 911. The colormap in the background represents GEMS glyoxal VCDs averaged from August 2020 to July 2021 at 00:45–07:15 UTC.

615

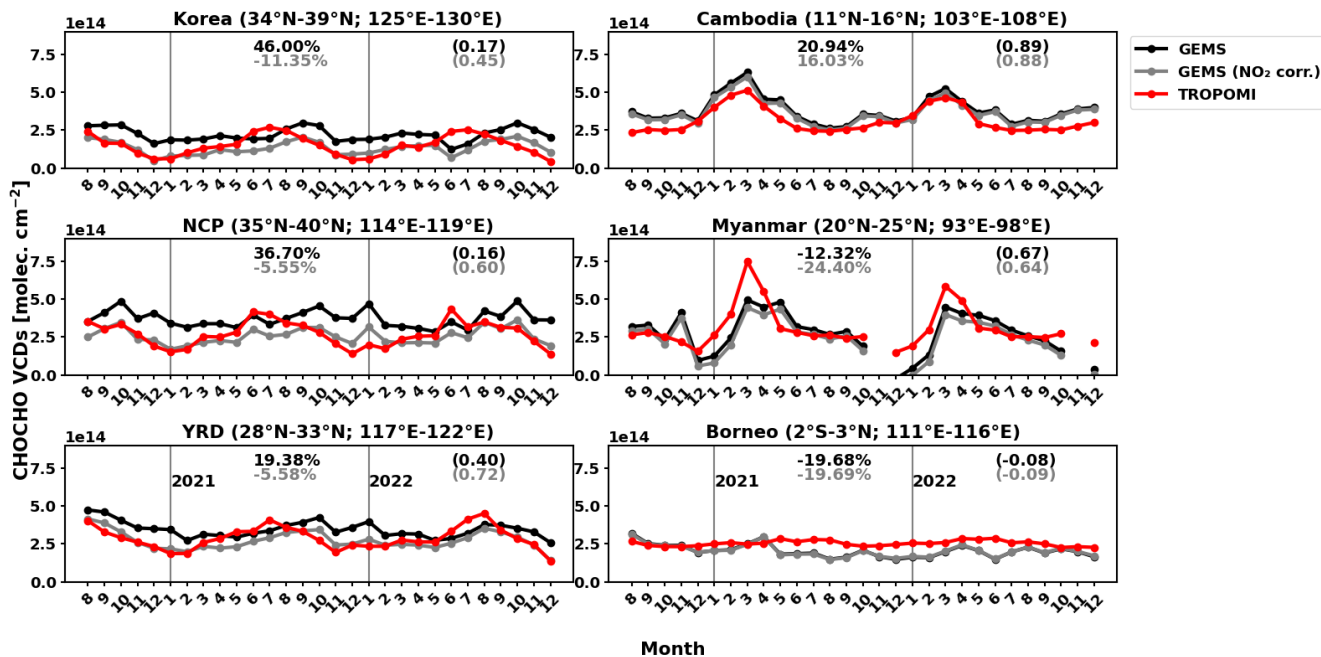
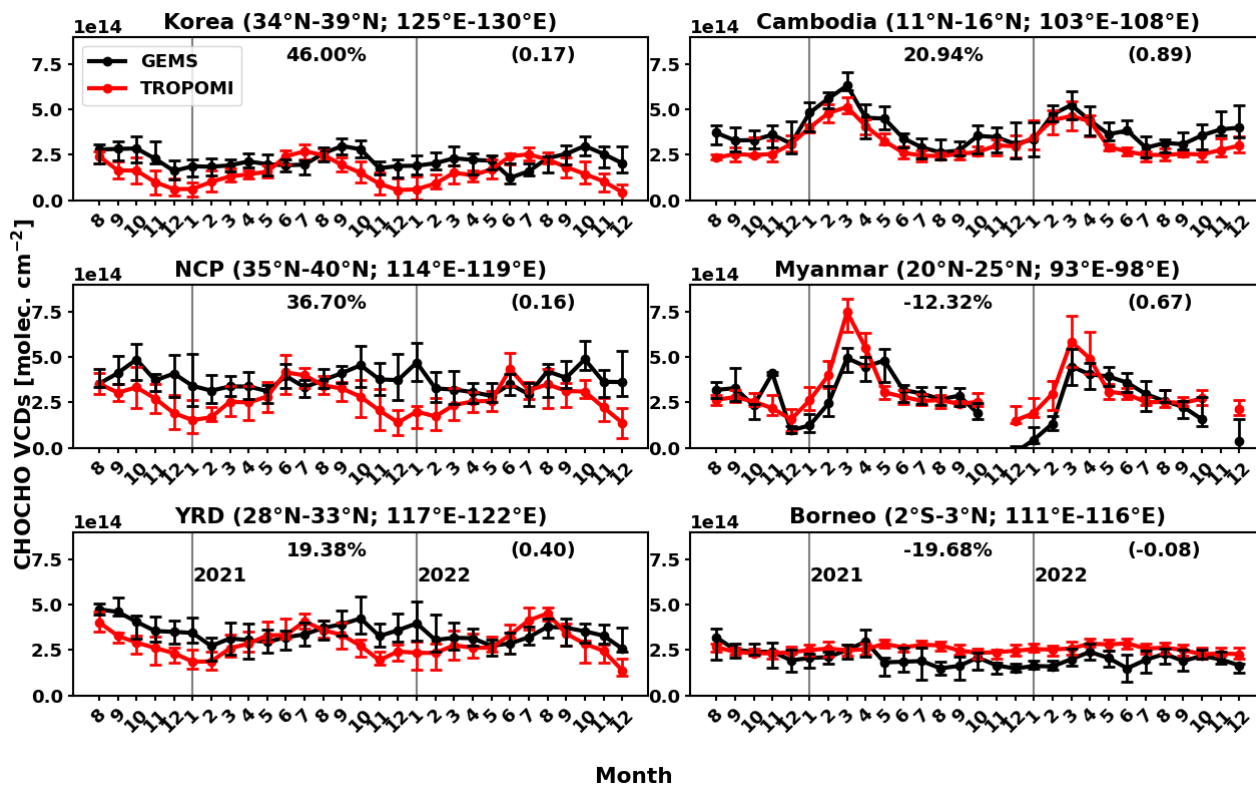
620



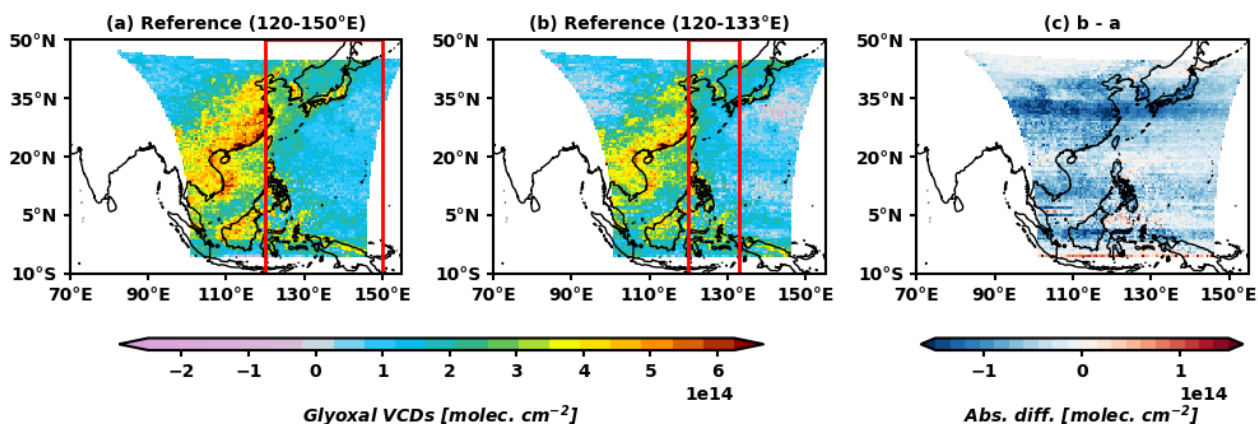
625

Figure 58. (a) GEMS and (b) TROPOMI glyoxal VCDs averaged from August 2020 to July 2021 at 11:30–15:30 local time. (c) The absolute difference between GEMS and TROPOMI glyoxal VCDs. Scatter plots comparing GEMS and TROPOMI glyoxal VCDs for the (d) whole domain, (e) Domain 1, and (f) Domain 2 indicated in Figure 4.7. GEMS VCDs depicted in this plot are the values without applying NO<sub>2</sub> correction described in Sect. 4.

630



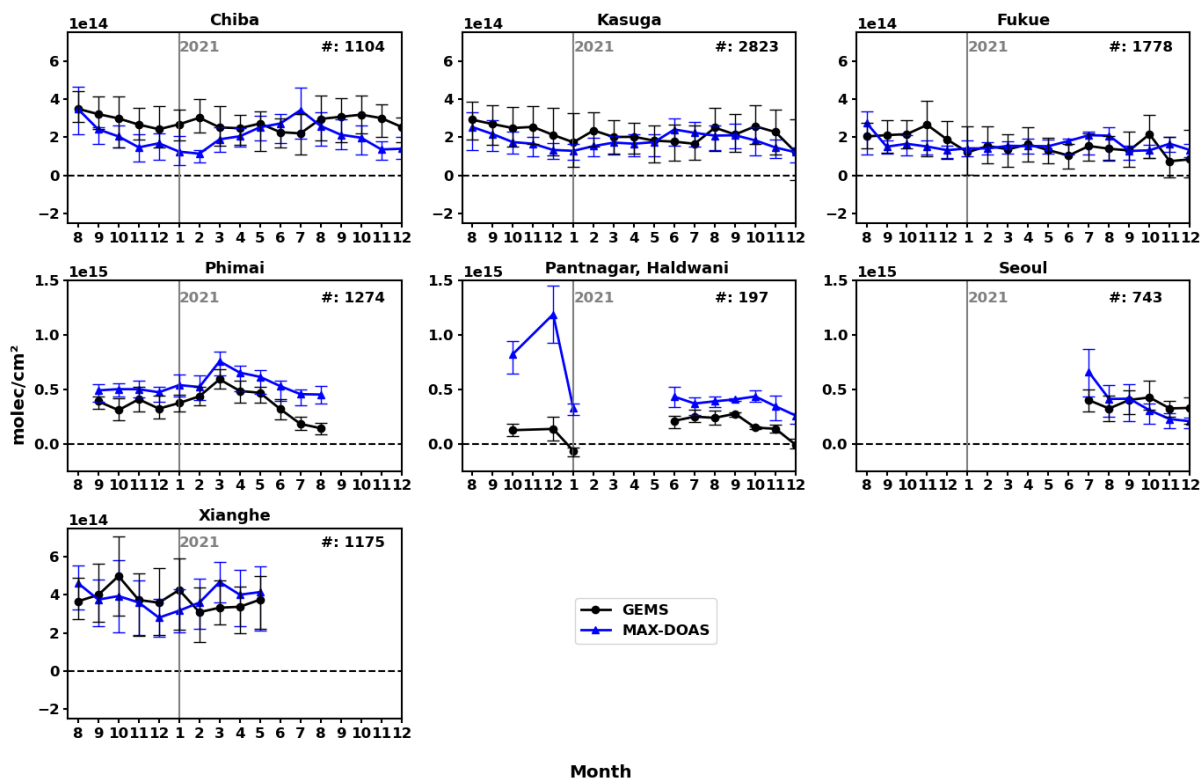
635 Figure 69. Monthly mean glyoxal VCDs from GEMS (black-line) and TROPOMI (red line) from August 2020 to December 2022 at  
 11:30–15:30 local time. The error bars indicate the black lines represent GEMS VCDs, the 25<sup>th</sup> and 75<sup>th</sup> percentiles of daily VCDs  
 averaged grey lines represent GEMS VCDs corrected for each domain depicted in Figure 4. NO<sub>2</sub>, and the red lines represent  
 TROPOMI VCDs. The numbers on the left denote the normalized mean bias of GEMS VCDs without (black) and with  
 respect (grey) NO<sub>2</sub> correction relative to TROPOMI VCDs, and the numbers in the parentheses in black and grey denote the  
 640 correlation coefficient of GEMS and TROPOMI VCDs.



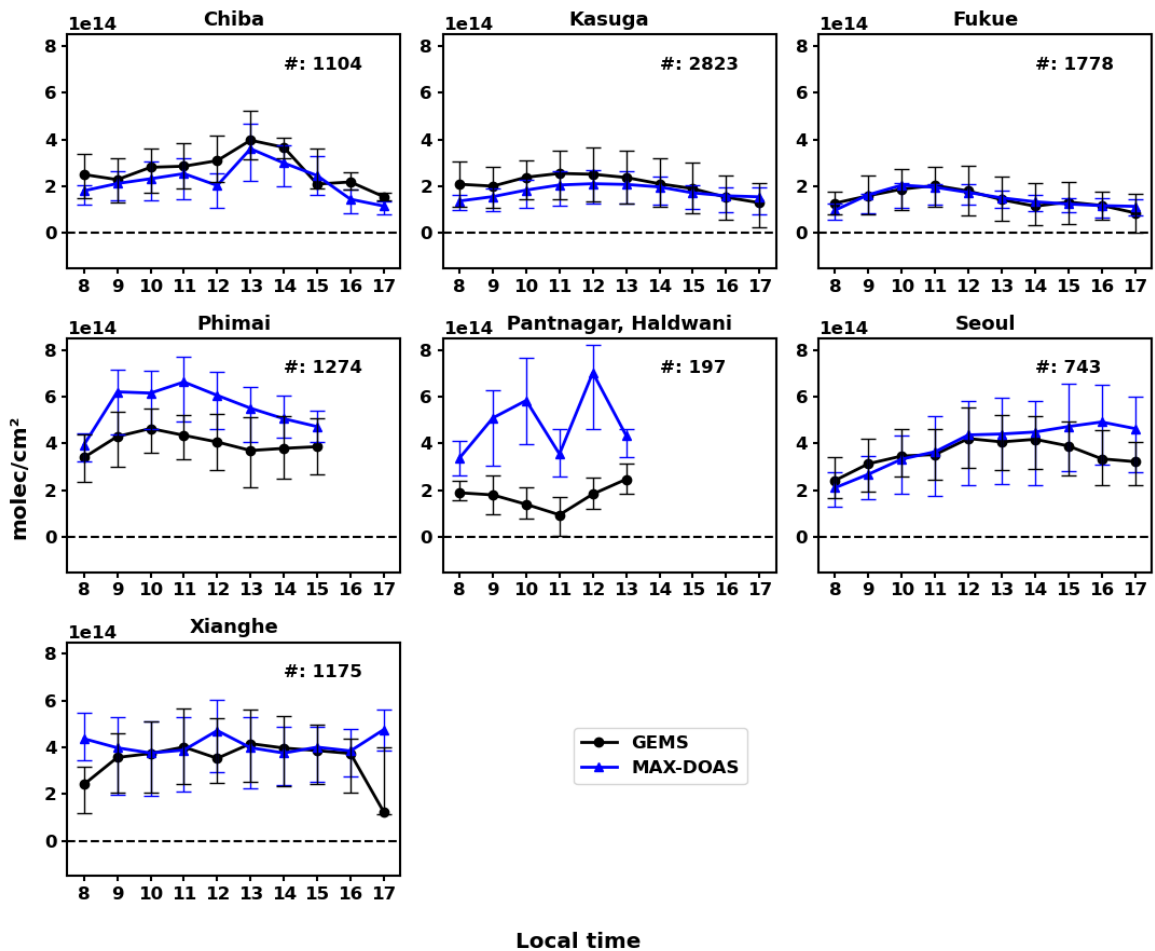
645 Figure 7. GEMS glyoxal VCDs averaged for the observations taken as nominal daily scan for 02:45–06:45 UTC in August 2020.  
 Panel A shows the VCDs retrieved without and with the reference sector of 120–133° E, and panel B shows those of 120–150° E.  
 The red boxes in panel a and b indicates reference sector used to retrieve each glyoxal VCDs. (c) The absolute difference between  
 panel a and b.  
 NO<sub>2</sub> correction, respectively.

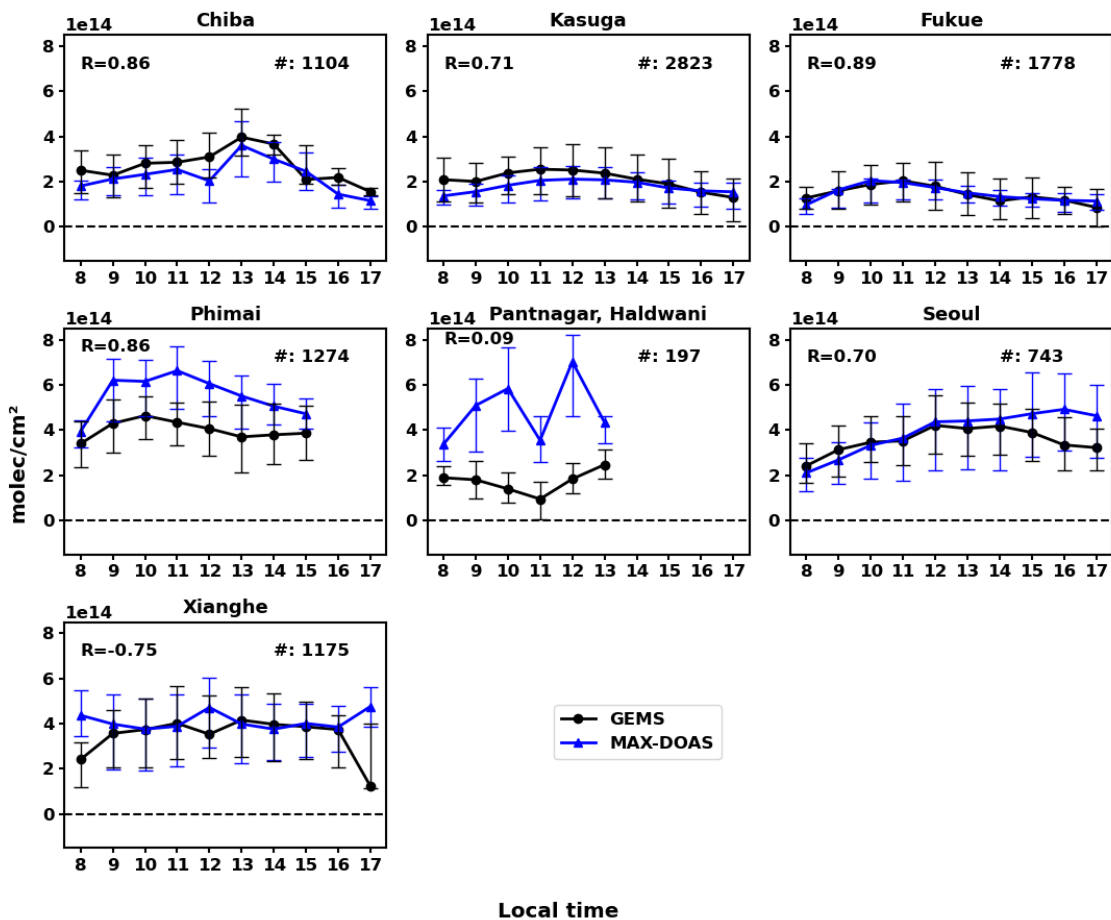
650





655 Figure 810. Monthly mean glyoxal VCDs from GEMS (black line) and MAX-DOAS (blue line) from August 2020 to December 2021. The error bars indicate the 25<sup>th</sup> and 75<sup>th</sup> percentiles of hourly averaged VCDs. The numbers on the right denote the number of hourly data co-located at each station.





660

Figure 911. Hourly mean glyoxal VCDs from GEMS (black line) and MAX-DOAS (blue line) from August 2020 to December 2021. The error bars indicate the 25<sup>th</sup> and 75<sup>th</sup> percentiles of hourly averaged VCDs. The numbers on the top left denote the diurnal correlation coefficients between GEMS and MAX-DOAS, and those on the top right denote the number of hourly data co-located at each station.

665